ORIGINAL PAPER

Martin Kroon · **Jakob Görtz** · **Shafiqul Islam** ·
Eskil Andreasson · **Viktor Petersson** · **Elin Persson Jutemar**

Experimental and theoretical study of stress relaxation in high-density polyethylene

© The Author(s) 2024

Abstract Stress relaxation of high-density polyethylene is addressed both experimentally and theoretically. Two types of stress relaxation testing are carried out: uniaxial tensile testing at constant test specimen length and compression testing of a 3D structure producing inhomogeneous deformation fields and relaxation. A constitutive model for isotropic, semi-crystalline polymers is also proposed. The model has the ability to model stress relaxation at different time scales. The developed model was implemented as a user subroutine in Abaqus (UMAT). The implicit integration scheme including an algorithmic tangent modulus is described in detail. The material model is calibrated by use of the uniaxial tensile tests, and the model is then validated by simulating the compression tests of the 3D structure. The model is able to describe the uniaxial tension tests well, and the comparison between the simulations and experimental testing of the 3D structure shows very good agreement.

1 Introduction

Polyethylene is one of the most common polymers and is used in a vast array of consumer goods. In fact, polyethylene and polypropylene represent about 92% of the synthetic plastics produced [23]. The mechanical behaviour of this polymer is therefore of great practical interest. In the present study, stress relaxation in a high-density polyethylene (HDPE) and under finite strain conditions is investigated both experimentally and theoretically.

Polyethylene (PE) that solidifies at rest forms a spherulitic microstructure, which is essentially isotropic from a mechanical point of view [28]. PE is a very ductile polymer and can be deformed up to 100% of straining

M. Kroon (✉)
Department of Mechanical Engineering, Linnaeus University, Växjö, Sweden
E-mail: martin.kroon@lnu.se

J. Görtz · S. Islam
Department of Mechanical Engineering, Blekinge Institute of Technology, Karlskrona, Sweden
E-mail: jakob.gortz@roxtec.com

S. Islam
E-mail: shafiqul.islam@bth.se

E. Andreasson · V. Petersson · E. Persson Jutemar
Tetra Pak, Lund, Sweden
E-mail: Eskil.Andreasson@tetrapak.com

V. Petersson
E-mail: Viktor.Petersson@tetrapak.com

E. Persson Jutemar
E-mail: Elin.PerssonJutemar@tetrapak.com

and beyond. At large strains, this means that the crystallites are disrupted, and the polymer chains align in the direction of deformation. The microstructural processes associated with large straining of HDPE and other semi-crystalline polymers have been documented in a number of studies (e.g. [3,4,10,21,28,38,39]). With regard to the macroscopic mechanical response, PE shows a strong strain rate dependence, and increasing strain-rate generally causes loss of ductility [19,50,57].

Due to its wide usage and industrial importance, polyethylene is one of the most investigated polymers. Different aspects of the mechanical behaviour of HDPE have been investigated in previous studies, including the response during monotonic loading [13,43,47,66] as well as during creep and relaxation loading [17,27,42,62].

In applications, polyethylene often undergo large deformations, and constitutive models based on a theory for finite strains are therefore needed. Many modelling approaches are based on the multiplicative decomposition of the deformation gradient into elastic and inelastic parts [11,30,37]. Some models are derived on the basis of microstructural considerations, and mixture theory is often used to account for the contributions from the amorphous and crystalline phases, e.g. Parks and Ahzi [46], Lee et al. [36], van Dommelen et al. [16], Nikolov et al. [43], Dusunceli and Colak [18], Selles et al. [56], and Sreejith et al. [63]. Most models, however, are more phenomenologically oriented, and many models have been proposed over the last years, e.g. Ayoub et al. [6], Zeng et al. [66], Balieu et al. [7], Pouriayevali et al. [48], Shojaei and Li [58], Uchida and Tada [65], Krairi and Doghri [29], Abdul-Hameed et al. [1], Garcia-Gonzalez et al. [22], Ayadi et al. [5], Barriere et al. [9], Qi et al. [49], Barba et al. [8], Felder et al. [20], Cundiff et al. [14], Hao et al. [25], Satouri et al. [55], Song et al. [61], Makki et al. [40], Reuvers et al. [51], Zeng et al. [67].

The models listed in the previous paragraph can all be said to be Lagrangian in the sense that they depend on measures of total and inelastic deformation. The model proposed here is Eulerian in the sense that all state variables are defined in the current state of the material (cf. [44]), and the evolution of elastic deformations is prescribed directly. The basic framework of the model has been established before (e.g. [2,32–35,52–54]). In these previous works, the same basic Eulerian framework has been applied for modelling residual stresses in metals during melting and solidification [32], general directional hardening [33], residual stresses at welds [35], volumetric inelasticity in semi-crystalline polymers [34], and stress relaxation and damage in semi-crystalline polymers [2]. In the present work, the ability to model stress relaxation at multiple time scales is added. The proposed model is calibrated by use of uniaxial tensile tests, both monotonic loading tests and stress relaxation tests. Relaxation at different initial stress levels and for different time periods is considered. The material model is also implemented in Abaqus as a user subroutine (UMAT), i.e. a fully implicit numerical implementation, including an analytic tangent modulus. The mechanical response of a 3D geometry is also tested experimentally, and these results are used to validate the material model.

The paper is organised as follows: Sect. 2 describes the experimental setups. The constitutive model is presented in Sect. 3. The new features of the proposed material model are demonstrated in Sect. 4. In Sect. 5, the material model is compared to and calibrated by use of uniaxial tensile test results. In Sect. 6, the UMAT implementation is validated by applying it to compression testing of a 3D structure. Section 7 contains a discussion and some concluding remarks.

2 Experiments

2.1 Uniaxial tensile tests

The uniaxial tensile stress relaxation tests used in the present work have been published previously in a master thesis [24]. These tests were performed on high-density polyethylene (HDPE), which is a semi-crystalline polymer. The HDPE used had a melt flow index of 26 g/10 min (190 °C, 2.16 kg) and a density of 0.953 g/cm^3. The test specimen used followed the standard ISO 527-2-1BA and is shown in Fig. 1. The specimen was flat with a rectangular cross-section, and the specimens were punched out from test plates with a thickness of $T_0 = 0.60$ mm. The test plates were manufactured through injection-moulding (ISO 294-5). The width of the specimen in the test region was $W_0 = 5.0$ mm and the initial distance between the grips in the testing machine was $L_0 = 60$ mm. The resulting initial cross-sectional area in the test region was $A_0 = W_0 T_0 = 3.0$ mm^2.

During the tests, force versus time was recorded using a load cell and a computer. The raw data from the tests consisted of force versus time data, $F(t)$, and load-line displacement versus time data, $\delta(t)$.

The information above is enough to establish the nominal stress vs. engineering strain relation for the different load cases and also the evolution of the engineering stress versus time at different constant engineering strain levels.
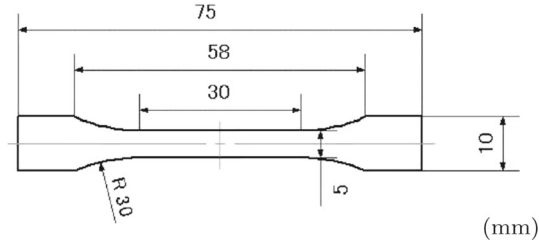
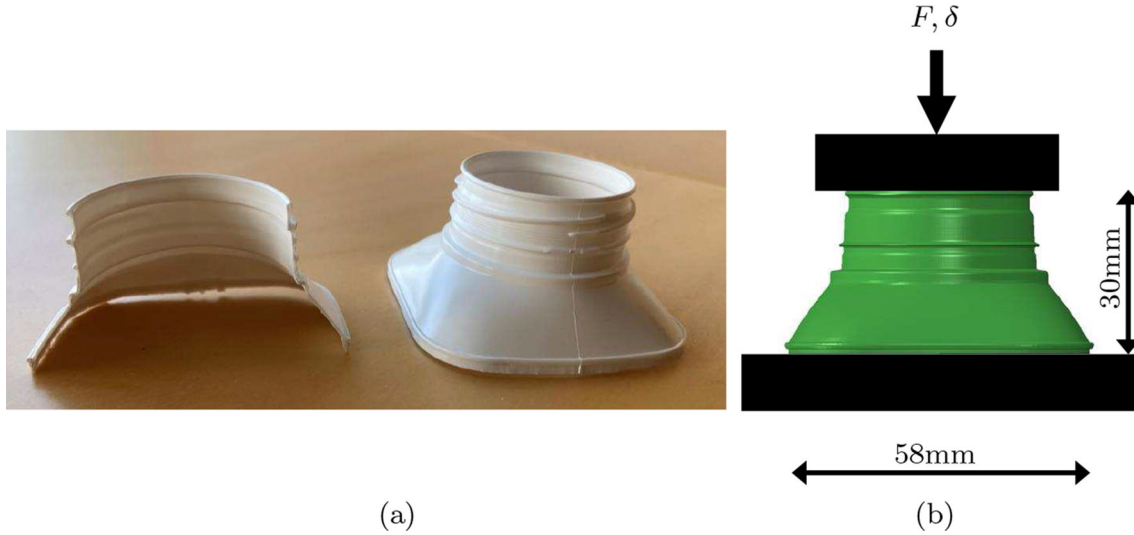**Fig. 1** Test specimen used in tensile tests

Fig. 2 3D geometry tested in compression

For all the tests, the grip separation rate was $\dot{\delta} = 30$ mm/min. This resulted in an engineering strain rate in the test specimens of $\dot{\delta}/L_0 = 0.00833$/s.

In the stress relaxation tests, the test specimen was first loaded up to a prescribed force, F_0. After that, the grip separation in the testing machine was kept constant, and the evolution of force, $F(t)$, was registered. Results from 5 different initial force levels are presented: $F_0 = 30$ N, 40 N, 60 N, 65 N, and 69 N. In general, three tests for each load-case were performed.

2.2 Compression testing of 3D geometry

A 3D geometry was also manufactured using injection-moulding and using the same material as in the uniaxial tensile testing, see Fig. 2. Figure 2a shows an example of the physical specimen, both the whole specimen and the cross-section of the specimen. Figure 2b shows the setup for the compression test. The 3D geometry was loaded in compression between two rigid blocks, as indicated in Fig. 2. The applied force, $F(t)$, and the load-line displacement, $\delta(t)$, were registered. The tests were performed in displacement control. The 3D geometry was loaded in compression up to a prescribed force F_0 and using the displacement rate $\dot{\delta} = 0.2$ mm/s. Two target forces were used: $F_0 = 150$ N and 200 N. Once the target force had been attained, the displacement was kept constant for a time of 3 h, allowing the geometry to relax, corresponding to a decreasing force $F(t)$. After 3 h, the geometry was unloaded by moving the cross-head of the testing machine back to $\delta = 0$ using the same displacement rate as during loading, i.e. $\dot{\delta} = -0.2$ mm/s.

3 Constitutive model

3.1 Kinematics

The position of a material point in the deformed configuration is denoted by the vector $\mathbf{x}$, and the velocity is $\mathbf{v} = \dot{\mathbf{x}}$, where $\dot{(\bullet)}$ denotes differentiation with respect to time. The velocity gradient $\mathbf{L}$ and the rate of deformation tensor $\mathbf{D}$ are defined by

$$\mathbf{L} = \frac{\partial \mathbf{v}}{\partial \mathbf{x}}, \quad \mathbf{D} = \frac{1}{2}(\mathbf{L} + \mathbf{L}^T). \tag{1}$$

The deformation state of the material is decomposed into its volumetric and distortional parts. The elastic distortional deformation is modelled by the symmetric, positive definite, unimodular tensor $\bar{\mathbf{B}}_e$ (i.e. $\det \bar{\mathbf{B}}_e \equiv 1$). The entity $\bar{\mathbf{B}}_e$ can be interpreted as the elastic left Cauchy–Green deformation tensor in the Lagrangian theory. The evolution of this tensor is given by

$$\dot{\bar{\mathbf{B}}}_e = \mathbf{L}\bar{\mathbf{B}}_e + \bar{\mathbf{B}}_e \mathbf{L}^T - \frac{2}{3}(\mathbf{D} : \mathbf{I})\bar{\mathbf{B}}_e - \Gamma \bar{\mathbf{A}}_p, \quad \Gamma \geq 0, \tag{2}$$

where $\mathbf{Q} : \mathbf{R} = \text{tr}(\mathbf{Q}\mathbf{R}^T)$ ($\mathbf{Q}$ and $\mathbf{R}$ are just two general second-order tensors), and $\mathbf{I}$ is the second order unit tensor. The first two terms in (2) on the right hand side can be seen as being related to objectivity. The third term ensures that $\bar{\mathbf{B}}_e$ remains unimodular, i.e. $\det \bar{\mathbf{B}}_e = 1$. Finally, the fourth term is where the actual constitutive behaviour comes into play. A detailed description of how the present Eulerian formulation of kinematics relates to the more standard Lagrangian formulations is provided in "Appendix A".

The rate of (distortional) inelastic deformations is defined by $\Gamma \geq 0$, which plays the role of the plastic multiplier in standard Lagrangian formulations of plasticity. The direction of inelastic deformations is determined by the tensor $\bar{\mathbf{A}}_p$, which takes the form

$$\bar{\mathbf{A}}_p = \bar{\mathbf{B}}_e - \left(\frac{3}{\bar{\mathbf{B}}_e^{-1} : \mathbf{I}}\right)\mathbf{I}, \tag{3}$$

where

$$\bar{\mathbf{A}}_p : \bar{\mathbf{B}}_e^{-1} = 0. \tag{4}$$

This choice of $\bar{\mathbf{A}}_p$ ensures that $\bar{\mathbf{B}}_e$ remains unimodular. Furthermore, in standard formulations of plasticity, the directions of plastic deformations are usually derived from a plastic potential (the yield criterion in the case of associative formulations). In the present formulation, the direction of plastic/inelastic deformations, $\bar{\mathbf{A}}_p$, is not related to any plastic potential but is simply prescribed directly according to (3).

Moreover, the volumetric part of the deformation, the dilatation J, evolves according to

$$\frac{\dot{J}}{J} = \mathbf{D} : \mathbf{I}. \tag{5}$$

In the present model, the yield criterion is formulated in strain space. The equivalent elastic distortional deformation, corresponding to the von Mises stress in stress-based formulations, is given by

$$\gamma_e = \frac{1}{2}\sqrt{\frac{3}{2}\bar{\mathbf{B}}_e' : \bar{\mathbf{B}}_e'}, \tag{6}$$

where

$$\bar{\mathbf{B}}_e' = \bar{\mathbf{B}}_e - \frac{1}{3}(\bar{\mathbf{B}}_e : \mathbf{I})\mathbf{I} \tag{7}$$

is the deviatoric part of $\bar{\mathbf{B}}_e$. Below, $(\bullet)'$ is used to denote the deviatoric part of $(\bullet)$, in accordance with the definition in (7). Also, the equivalent rate of total distortional deformation is defined as

$$\dot{\varepsilon} = \sqrt{\frac{2}{3}\mathbf{D}' : \mathbf{D}'}, \tag{8}$$

where $\mathbf{D}'$ is the deviatoric part of $\mathbf{D}$.

3.2 Strain energy and stress

The strain energy of the material, Σ, defined per unit mass, is taken to be

$$\rho_0 \Sigma = \frac{\mu}{2}(\alpha_1 - 3) + \frac{K}{2}(J - 1)^2, \tag{9}$$

i.e. a standard neo-Hookean material is adopted. Above, ρ_0 is the density of the material in the reference configuration, $\alpha_1 = \bar{\mathbf{B}}_e : \mathbf{I}$ is the first invariant of $\bar{\mathbf{B}}_e$, and μ and K are the positive shear and bulk moduli of the material. The dilatation, J, is taken to be purely elastic, i.e. inelastic deformations are taken to be incompressible.

Assuming isothermal conditions, the rate of material dissipation requires that

$$\mathbf{T} : \mathbf{D} - \rho \dot{\Sigma} = \ldots = \left\{ \mathbf{T} - \frac{\rho}{\rho_0} \left(\mu \bar{\mathbf{B}}_e' + K(J - 1)J\mathbf{I} \right) \right\} : \mathbf{D}$$
$$+ \frac{\rho \mu}{2\rho_0} \Gamma (\bar{\mathbf{A}}_p : \mathbf{I}) \geq 0, \tag{10}$$

where $\mathbf{T}$ is the symmetric Cauchy stress, and $\rho = \rho_0/J$ is the current density of the material. The Cauchy stress is taken to be

$$\mathbf{T} = \frac{\mu}{J} \bar{\mathbf{B}}_e' + K(J - 1)\mathbf{I}, \tag{11}$$

and the von Mises stress σ_e is defined by

$$\sigma_e = \sqrt{\frac{3}{2} \mathbf{T}' : \mathbf{T}'}. \tag{12}$$

In the last term of (10), μ, ρ, ρ_0, and Γ are all positive constants or variables. Also, since $\bar{\mathbf{B}}_e$ is unimodular, $\bar{\mathbf{A}}_p : \mathbf{I} \geq 0$ holds. Taken together, these properties ensure that the dissipation in (10) is always non-negative.

For the numerical implementation of the model, to be discussed in a later section, the Kirchhoff stress, $\boldsymbol{\tau}$, is also introduced as

$$\boldsymbol{\tau} = J\mathbf{T}, \tag{13}$$

and when comparing the model to experiments, the first Piola–Kirchhoff stress is used, i.e.

$$\mathbf{P} = \boldsymbol{\tau} \mathbf{F}^{-T}, \tag{14}$$

where $\mathbf{F}$ is the deformation gradient.

3.3 Inelastic deformations

The rate of inelastic deformations, Γ, is expressed as

$$\Gamma = \Gamma_{vp} + \Gamma_r, \tag{15}$$

where Γ_{vp} accounts for short-term viscoplasticity, and Γ_r accounts for long-term stress relaxation. The specific forms for Γ_{vp} and Γ_r are chosen according to

$$\Gamma_{vp} = (a_0 + b_0 \dot{\varepsilon}) \langle \gamma_e - \kappa \rangle, \tag{16}$$

$$\Gamma_r = \sum_{i=1}^{n} c_i \langle \gamma_e - \zeta_i \rangle, \tag{17}$$

where κ and ζ_i are hardening variables, and a_0, b_0, and c_i are material constants. Specifically, a_0 and b_0 govern the rate-dependent and rate-independent short-term inelastic response of the material, respectively, whereas c_i can be seen at time constants for the relaxation behaviour of the material. The model is taken to consist of n relaxing terms/units, which enables modelling of stress-relaxation at different time-scales. The hardening

variable κ models isotropic hardening in strain space. The hardening variables ζ_i are more abstract, but model a type of hardening associated with the relaxation in the material.

The Macaulay brackets $\langle \bullet \rangle$ are defined by

$$\langle x \rangle = \max(x, 0). \tag{18}$$

The evolution of the hardening variables κ and ζ_i are governed by the functions

$$\dot{\kappa} = \xi \Gamma_{vp}, \tag{19}$$

$$\dot{\xi} = m \Gamma_{vp}(\xi_s - \xi), \tag{20}$$

$$\dot{\zeta}_i = n_i \dot{\varepsilon}(\zeta_{s,i} - \zeta_i) \cdot \Theta(\gamma_e - \zeta_i), \tag{21}$$

where $m \geq 0$ and $n_i \geq 0$ are hardening rates, $\zeta_{s,i}$ are the saturated values of the hardening variables, and $\Theta(\bullet)$ is the Heaviside step function. The rate of the evolution of κ is governed by the additional state variable ξ, which evolves to the saturated value ξ_s. This is a convenient way to model the hardening of the present material. The initial values of the respective hardening variables are denoted by κ_0, ξ_0, and ζ_{i0}.

In principle, (20) can be solved analytically, such that ξ is expressed as a function of the time integral of Γ_{vp}. But in the present implementation (as will be shown below), the differential relation in (20) is used, since history variables are avoided in the present model formulation.

3.4 Summary of material model

The model contains the following state variables and non-standard kinematic entities:

- $\bar{\mathbf{B}}_e$: elastic distortional deformation
- α_1: first invariant of $\bar{\mathbf{B}}_e$
- J: elastic dilatational deformation
- $\mathbf{A}_p$: direction of inelastic deformation
- Γ: rate of inelastic deformation
- Γ_{vp}: rate of short-term viscoplasticity
- Γ_r: rate of long-term stress relaxation
- κ: isotropic hardening
- ξ: state variable controlling the rate of isotropic hardening
- ζ_i: relaxation hardening
- γ_e: equivalent distortional elastic deformation
- $\dot{\varepsilon}$: equivalent rate of total distortional deformation

  In addition, the model contains the following model parameters:

- μ: shear modulus
- K: bulk modulus
- a_0: controls the rate of rate-dependent viscoplasticity
- b_0: controls the rate of rate-independent plasticity
- m: controls the rate of isotropic hardening
- c_i: controls the rate of relaxation
- n_i: controls the rate of relaxation hardening
- ξ_s: maximum rate of isotropic hardening
- $\zeta_{s,i}$: saturated value of relaxation hardening

4 Model behaviour in simple load cases

The behaviour of the proposed model is illustrated for some simple load cases, i.e. uniaxial tension, biaxial tension, and simple shear. The numerical implementation of these simple load cases is described in "Appendix B". Uniaxial and biaxial loading are applied in terms of a prescribed strain ε_{11} ($\varepsilon_{22} = \varepsilon_{11}$ for biaxial loading), and for simple shear, the shear angle γ is instead prescribed. The shear modulus and Poisson's ratio were set to $\mu = 300$ MPa and $\nu = 0.4$, respectively. This gives a bulk modulus of $K = 2\mu(1+\nu)/3(1-2\nu) = 1400$ MPa. These elastic constants are listed in Table 1.

By use of Γ_{vp}, rate-independent as well as rate-dependent inelasticity can be modelled. Yielding starts when γ_e exceeds κ_0. The material hardening is modelled by κ, and the hardening rate is governed by m and the state variable ξ. The parameter a_0 models the viscoplasticity, and b_0 governs the rate-independent plasticity. The set of viscoplastic model parameters that is used in this study of the model behaviour is listed in Table 2.

The ability to model stress relaxation at different time scales is a new aspect of the present model. The contribution of Γ_r is therefore demonstrated. Figure 3 shows the stress response when the strain is increased quickly and then held at a constant level. The elasticity constants in Table 1 and the viscoplasticity parameters in Table 2 are applied. For the stress relaxation behaviour, only one relaxation term is used ($n = 1$), and $\zeta_{s,1} = 0.06$.

The Γ_r-term causes stress relaxation. The relaxation behaviour for three different choices of c_1 is shown, i.e. $c_1 = 1/s$ (solid lines), 3/s (dashed lines), and 10/s (dotted lines). Two values of the hardening rate n_1 are explored, i.e. $n_1 = 1$ (blue lines) and 10 (red lines). It is clear from Fig. 3, that increasing c_1 causes the stress to relax faster to the equilibrium stress level. Also, increasing n_1 causes the equilibrium stress level to increase.

More relaxation units are now activated, and the three relaxation units listed in Table 3 are added to the model parameters. The elastic constants in Table 1 together with the inelasticity parameters in Tables 2 and 3 together constitute the set of model parameters that provided the best fit of the model to the experimental data, as will be shown in the next section. For now, the proposed model is explored a bit further for different types of loading.

Figure 4 shows the response of the model for some different simple load-cases. Figure 4a shows the response of the model in uniaxial tension, biaxial tension, and simple shear during cyclic loading. The material is first loaded well into the plastic regime, then unloaded and reloaded in compression or the opposite shearing direction in the case of simple shear. The material is then unloaded and reloaded in tension/positive shearing again. As expected, the curve for biaxial loading (red line) produces the highest stresses, whereas simple shear produces the lowest stresses (green line).

Figure 4b demonstrates the model response in the case of repeted loading in uniaxial tension. The material is first loaded up to a strain of $\varepsilon_{11} = 0.2$, then unloaded to 0.18, reloaded to 0.4, unloaded to 0.38, etc.

Table 1 Parameters for elastic behaviour

μ (MPa)	ν (–)	K (–)
300	0.4	1400

Table 2 Parameters for viscoplastic behaviour

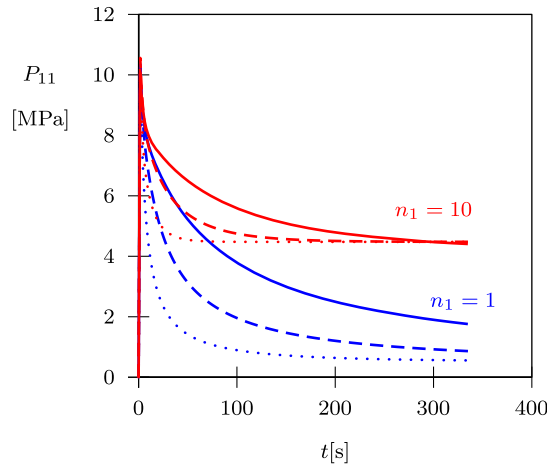| a_0 (1/s)	b_0 (–)	κ_0 (–)	m (–)	ξ_0 (–)	ξ_s (–)
3	1200	0.005	1.3	0.021	0.0006

Fig. 3 Parametric study for the relaxation behaviour (parametres in Tables 1 and 2 applied): $n_1 = 1$ (blue lines) and $n_1 = 10$ (red lines); $c_1 = 1/s$ (solid lines), $c_1 = 3/s$ (dashed lines), $c_1 = 10/s$ (dotted lines) (Color figure online)

Table 3 Parameters for relaxation

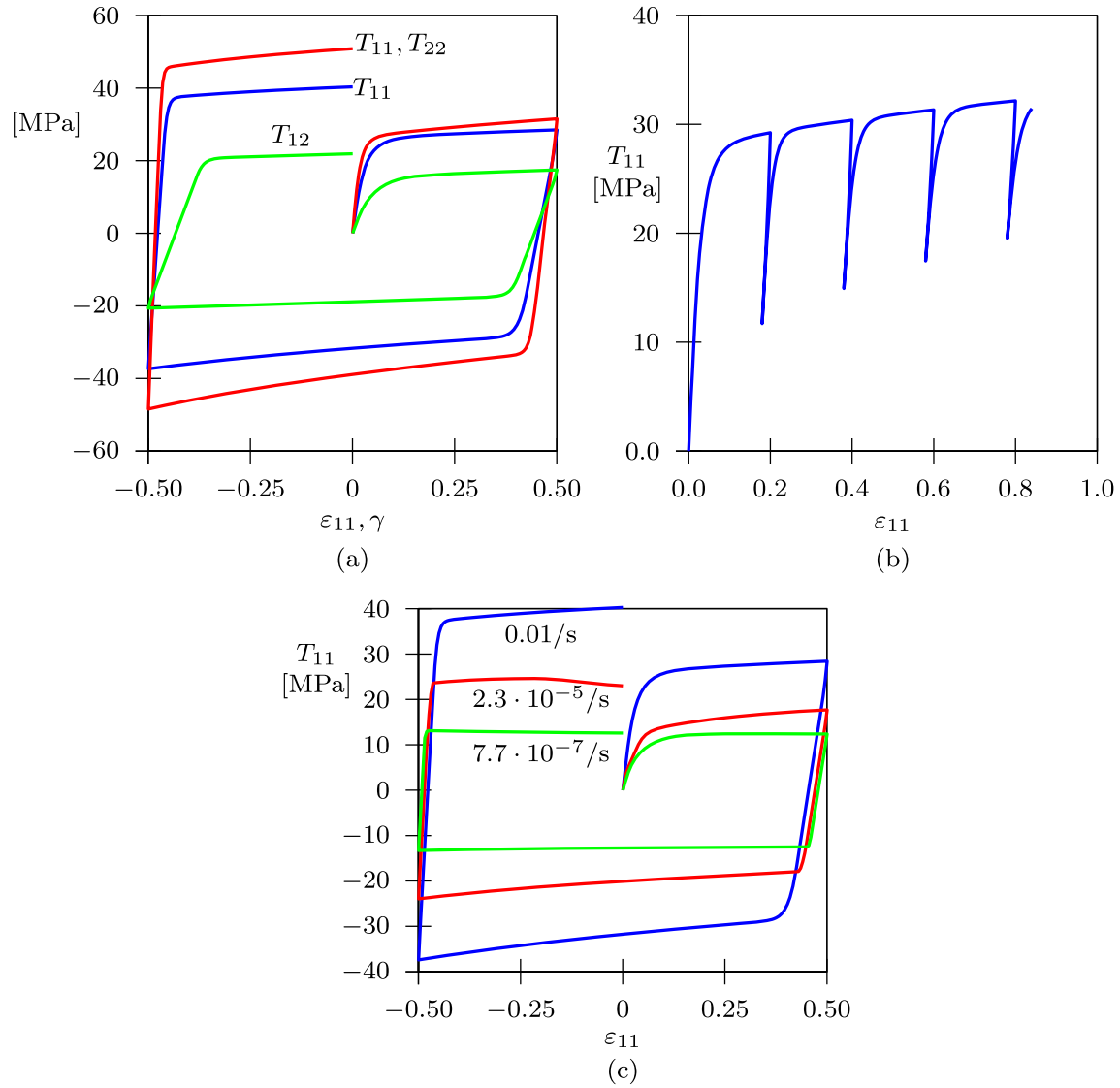| c_1 (1/s)	c_2 (1/s)	c_3 (1/s)
1	0.05	0.00003
n_1 (–)	n_2 (–)	n_3 (–)
9	26	2.5
$\zeta_{s,1}$ (–)	$\zeta_{s,2}$ (–)	$\zeta_{s,3}$ (–)
0.06	0.02	0.1

Fig. 4 Model responses using the parameters in Tables 1, 2 and 3: **a** responses in uniaxial tension (blue line), biaxial tension (red line), and simple shear (green line) (loading rate: $\dot{\varepsilon}_{11} = \dot{\gamma} = 0.01$/s); **b** uniaxial tension response during repeated cyclic loading ($\dot{\varepsilon}_{11} = 0.1$/s); **c** uniaxial tension response for loading rates $\dot{\varepsilon}_{11} = 0.01$/s (blue line), 2.3×10^{-5}/s (red line), and 7.7×10^{-7}/s (green line) (Color figure online)
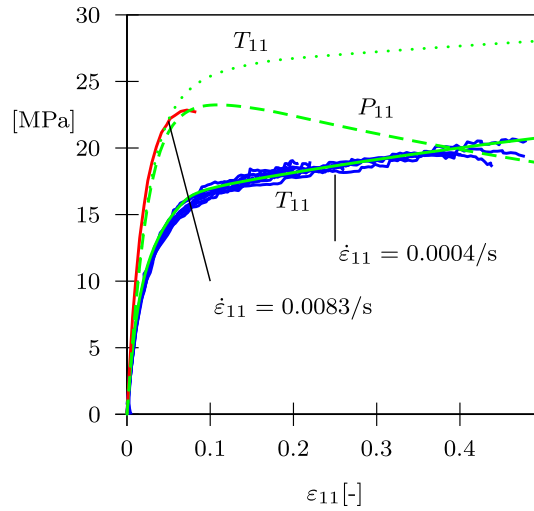
Fig. 5 Stress–strain response in monotonic uniaxial tensile tests. Strain-rates: $\dot{\varepsilon}_{11} = 0.0004$/s (experiments: blue lines, model prediction: green solid line), and $\dot{\varepsilon}_{11} = 0.0083$/s (experiments: red line, model prediction: green dashed and dotted lines) (Color figure online)

Figure 4c again shows a case of cyclic loading in uniaxial tension but in this case for three different loading rates. The first loading rate ($\dot{\varepsilon}_{11} = 0.01$/s, blue line) is a moderate loading rate, where short-term viscoplasticity primarily governs the material response. The other two lines (red and green) show the model response at lower loading rates where stress relaxation comes into play. The red and green lines represent the cases $\dot{\varepsilon}_{11} = 2.3 \times 10^{-5}$/s and 7.7×10^{-7}/s, respectively, which correspond to completing the load cycle in 24 h and in 30 days, respectively. It is clear from Fig. 4c that stress relaxation generally decreases the magnitude of the stress levels during the load cycle.

5 Model calibration

5.1 Prerequisites

The proposed constitutive model was calibrated using experimental uniaxial tensile tests. Two types of tests were used: monotonic loading at constant strain rate and relaxation testing at fixed test specimen length. These test data came from two sources: the master thesis by Görtz [24] that was described in Sect. 2, and another experimental study by Abelen and Kroon [2] on the same material. Görtz [24] performed testing both in terms of monotonic loading at constant strain rate as well as stress relaxation testing. The output from this study was nominal/engineering stress versus either strain or time. In the study by Abelen and Kroon [2], digital image correlation (DIC) was used to establish the true stress in the specimen, and this study produced data in terms of true (Cauchy) stress versus strain. The data from Görtz [24] are therefore represented by the first Piola–Kirchhoff stress, P_{11}, whereas the data from Görtz [2] come in terms of the Cauchy stress, T_{11}. These data are compared to the corresponding stress measures from the model.

5.2 Comparison with uniaxial tensile tests

The model is first compared to the monotonic stress–strain tests and also the relaxation tests. As indicated above, the model parameters that provided the best fit to the experimental data are listed in Tables 1, 2 and 3. Three terms in the expression for Γ_r were needed to be able to fit all of the relaxation data ($n = 3$). The optimisation of the model parameters was performed manually. When plotting the results, the engineering strain, $\varepsilon_{11} = F_{11} - 1$, is again used. Stresses are represented both by the Cauchy stress, T_{11}, and the nominal/engineering stress, P_{11}, as indicated above.

In Fig. 5, the experimental results for the case of monotonic loading at two different loading rates are shown together with the model response. The result for the higher loading rate is from Görtz [24] and the result for the lower loading rate is from Abelen and Kroon [2]. In the tests with the lower loading rate, 8 specimens

were tested, and DIC (digital image correlation) and manual thickness measurements of the specimens during the test enabled determination of the true stress–strain response. The dispersion in these results (blue lines) is very low, as can be seen in Fig. 5. The uniaxial test carried out in Görtz [24] only included measurement of the evolution of the force, and together with the initial cross-sectional area, the nominal stress could be established. As can be seen in Fig. 5, the true stress (solid green line) increases monotonically with the strain, whereas the nominal stress (green dashed line) reaches a peak and then starts to decrease (both in experiments and model prediction). The calibrated model is able to reproduce the stress–strain responses in the experiments very well at both loading rates.

The data from Görtz [24] (red line) are only shown up to the point of necking, since beyond necking, the engineering stress–strain results are more or less meaningless (unless the necking behaviour is analysed in more detail). The associated model prediction (dashed green line) reaches a peak and then decreases. It is emphasised, that this decrease in the model prediction is related to the fact that cross-sectional area changes are not accounted for in the engineering stress, and hence, this decrease in the numerical prediction has nothing to do with necking. (We are just simulating one material element and not the whole test specimen.) Furthermore, the green dotted line is the predicted true stress response at the higher loading rate, illustrating that the (predicted) true stress increases monotonically also at the higher loading rate.

In the relaxation tests, the material was loaded at a specified deformation rate up to a prescribed force, and then the grips in the testing machine were kept fixed. The force relaxation was registered. Figure 6a–d demonstrate the outcome from these tests together with the fitted model response. Results are shown in terms of nominal stress, P_{11}, versus time. In most of these tests, 3 tests were performed for each load-case, except for the long-term test in Fig. 6d, where only two tests were performed. The experimental data points in Fig. 6a–d represent the average results from the tests. The dispersion in these tests was very low.

The short-term stress relaxation is shown in Fig. 6a, i.e. stress relaxation during the first 350 s. The agreement between experiments and model is excellent for the two lower load-cases. For the two higher load-cases, the model overpredicts the initial relaxation somewhat. Figure 6b shows a close-up of the response of the material during the first 100 s. Overall, the model does a good job of predicting the initial relaxation observed in the tests.

The medium-long stress relaxation is shown in Fig. 6c. In this case, there are only three load cases. The agreement between model and experiments is generally good, even though the long-term stress level is slightly overestimated by the model in the lowest load case.

In Fig. 6d, the long-term relaxation behaviour is shown. Due to the length of this experiment, it was only carried out for one force level, i.e. $F_0 = 65$ N. As can be seen from Fig. 6d, the agreement between model and experiments is good.

In Fig. 6a, c, and d reference curves (dashed lines) are also included. These curves show what the predicted response would be if the relaxation is turned off. The dashed lines in Fig. 6a shows the outcome for the respective load levels if $c_1 = c_2 = c_3 = 0$ is applied. There is some relaxation present anyway, which is associated with viscoplasticity and the parameter a_0. However, the continued stress relaxation cannot be captured if c_1, c_2, and c_3 are turned off.

The dashed lines in Fig. 6c show the outcome if c_1 is set according to Table 3, but $c_2 = c_3 = 0$ is applied. In this case, the mid-range relaxation behaviour cannot be properly captured. Finally, the orange dashed line in Fig. 6d illustrates the outcome for the case $F_0 = 65$ N when c_1 and c_2 are chosen according to Table 3 but c_3 is turned off. The long-term relaxation is not captured by the model then.

6 Model validation using 3D geometry

6.1 Preliminaries

The material model was implemented in Abaqus [26] as a user subroutine (UMAT). The numerical implementation of the stress update algorithm and the consistent (algorithmic) tangent stiffness is described in detail in "Appendix C".

6.2 Problem formulation

The implemented model is applied to the problem illustrated in Fig. 7, i.e. the compression test of a 3D geometry is simulated. The FE representation of the 3D geometry is shown in Fig. 7a, and the FE problem
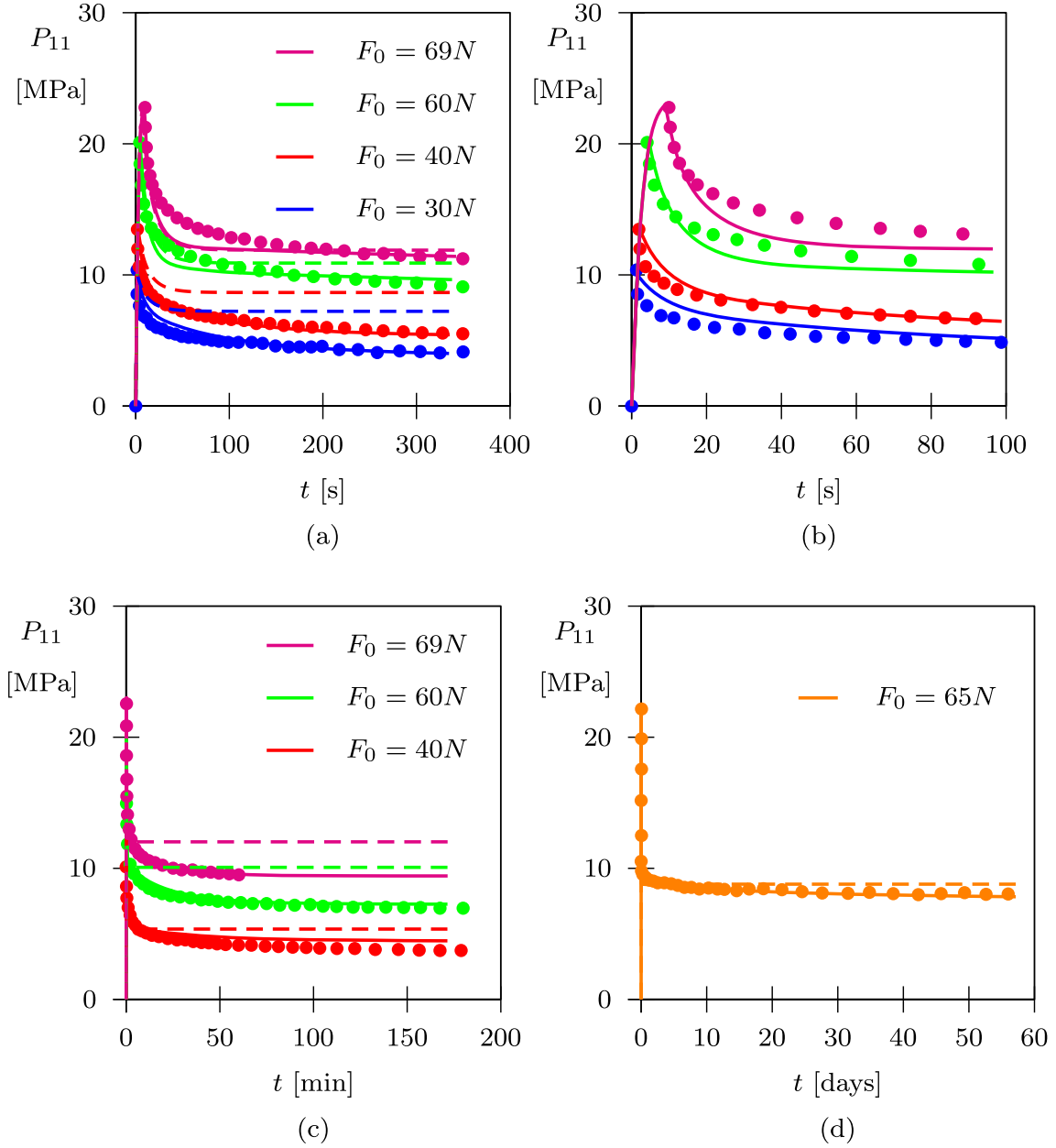
Fig. 6 Comparison between experiments (symbols) and model predictions (solid lines) for relaxation tests: **a** short-term response for $F_0 = 30$ N (blue), 40 N (red), 60 N (green), and 69 N (magenta); **b** close-up of the first 100 s of the short-term response in (**a**); **c** medium-long response for $F_0 = 40$ N (red), 60 N (green), and 69 N (magenta); **d** long-term response for $F_0 = 65$ N (orange) (Color figure online)

to be solved is shown in Fig. 7b. The geometry is placed between to rigid blocks. The contact between the HDPE geometry and the rigid blocks is taken to be friction-less. The whole geometry was discretized using about 89,000 8-node linear elements, and the analyses were carried out as quasi-static, implicit simulations. The simulations of the compression tests took about 4 h on a standard computer (no parallelization), and on the average about 60 load increments were used to simulate the loading-unloading procedure.
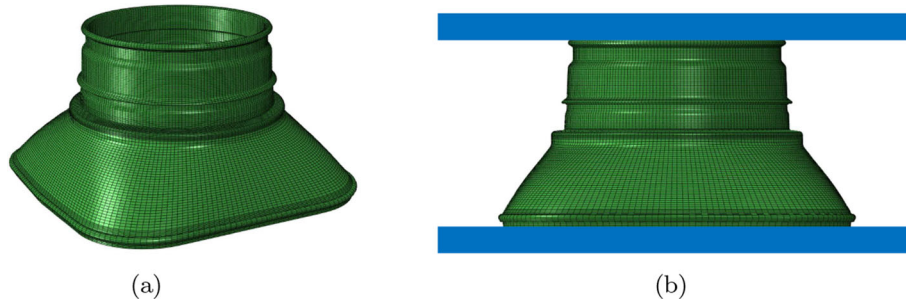
(a)   (b)

Fig. 7 a Mesh of 3D geometry; **b** FE problem

6.3 Results

The compression tests described in Sect. 2 were simulated. Figure 8 shows contours of the von Mises stress, σ_e, and the hardening variable, κ, at different stages of the simulation. A cross-section of the geometry is shown, i.e. the interior of the geometry is seen. Just as in the experiments, the displacement rate during loading and unloading was $\dot{\delta} = 0.2$ mm/s.

At $t = 0$, the whole geometry is stress-free and no hardening has taken place, i.e. $\kappa = \kappa_0 = 0.005$. At time $t = 6.4$ s, the target force, $F_0 = 200$ N, has been reached. This is the point when the structure experiences the highest stresses, and the peak stress reaches a value of about 25 MPa. Some inelastic deformations have taken place, and some hardening has taken place. For $t > 6.4$ s, the applied displacement, δ, is kept constant, and the structure experiences stress relaxation. At the end of the relaxation phase, at $t = 3$ h, the applied force has decreased to a value of about 77 N, which is less than half of F_0. During the relaxation phase, inelastic deformations take place, which results in material hardening. The peak value of κ is about 0.025 at the end of the relaxation phase. The last stage of the loading cycle consists of unloading of the geometry. Some parts of the structure have undergone significant inelastic deformations and associated material hardening. However, this does not result in any significant residual stresses after the external load has been removed, as can be seen in the lowest figure in Fig. 8.

Figure 9 shows comparisons between the simulations and experiments in terms of the force response during tests with $F_0 = 150$ N and 200 N. Three tests were performed for each target stress F_0. The experimental results are indicated by solid blue lines ($F_0 = 150$ N) and solid red lines ($F_0 = 200$ N). Model predictions are indicated by magenta dashed lines ($F_0 = 150$ N) and green dashed lines ($F_0 = 200$ N).

Figure 9a shows the evolution of the force, F, as a function of time, t. Time goes from 0 to 3 h, which means that the initial loading phase is hardly visible. For the case $F_0 = 200$ N, the force starts at 200 N and decreases down to about 77 N after 3 h. In other words, the material experiences significant stress relaxation. The three experimental curves (solid red lines) are well collected. The model overestimates the initial relaxation compared to the experiments, but at the end of the relaxation process, the model prediction is quite close to the experimental stress level. The same conclusions hold for the case $F_0 = 150$ N, i.e. the experimental results show a low dispersion. The force decreases from 150 N to about 60 N at the end of the relaxation process. The model again overestimates the initial relaxation, but at the end of the relaxation phase, the model agrees very well with the experimental force level.

Figure 9b essentially shows the same information as in Fig. 9a, but in Fig. 9b, the horizontal axis shows the logarithm of time instead. In Fig. 9b, it can be seen that in the very beginning of the relaxation process, the model actually underestimates the relaxation, but after about 100 s the model instead starts to overestimate the relaxation. It should also be noted that the experimental curves have been translated in the horizontal direction (t-dimension) so that they reach the peak force at the same time as the simulations.

In Fig. 9c, force versus displacement results are shown. In this diagram, it can be seen even more clearly that the experimental curves exhibit an initial non-linearity. In the experiments, the specimens always undergo some initial adjustments, which causes this initial non-linearity. Again, in order to help the comparison between model and experiments, the experimental curves were shifted in the displacement dimension so that the peak force in the experiments appears at the same displacement as in the simulations. In the force-displacement diagram, the experimental curves show some dispersion. The overall impression is that the model seems to somewhat underestimate the initial stiffness of the structure. As noted earlier, the total amount of relaxation is very well predicted by the model. From Fig. 9c it is also evident that the final unloading path is relatively
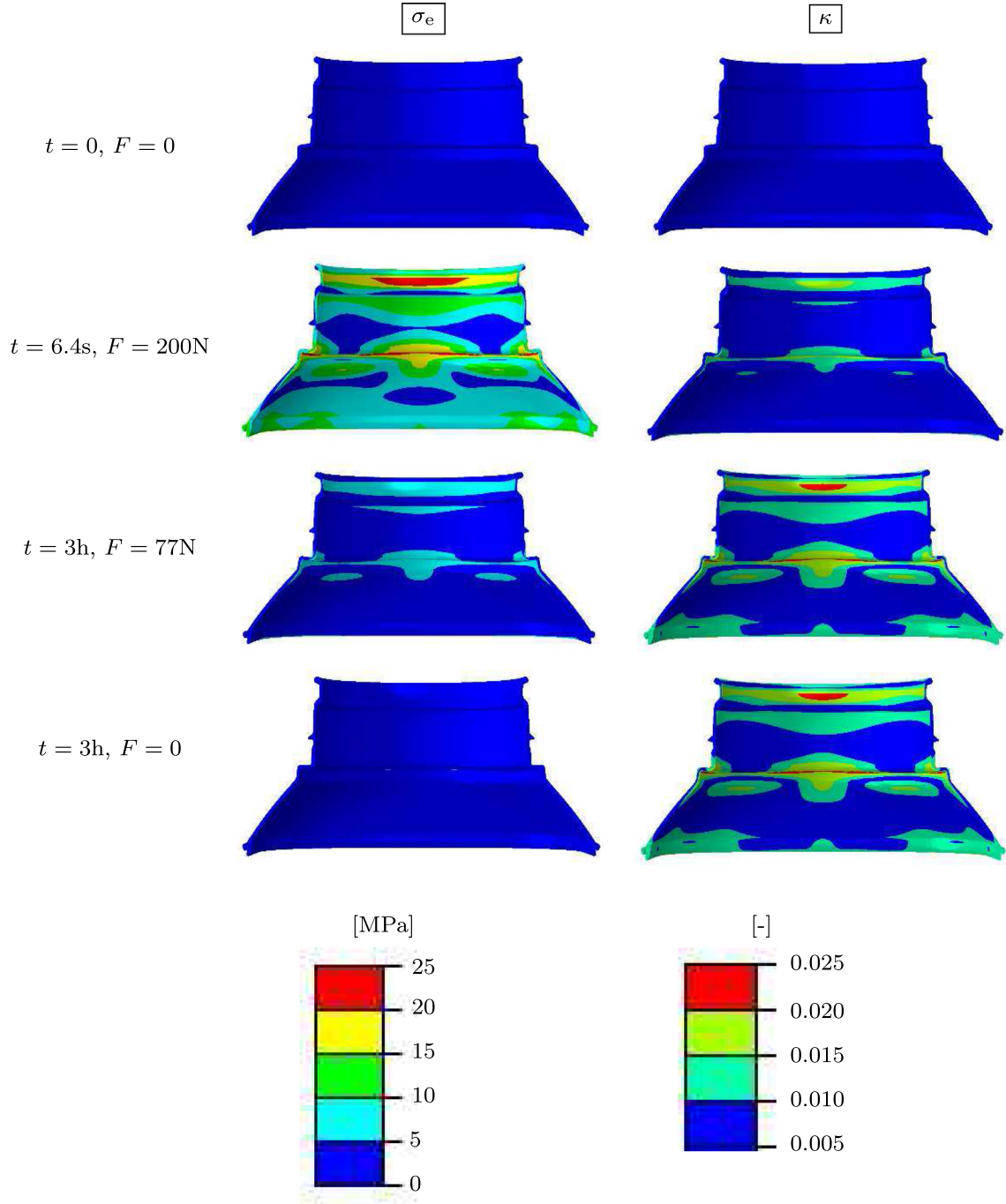
Fig. 8 Contours of σ_e and κ for a load cycle with $F_0 = 200$ N

well predicted by the model. The experiments show a non-linear unloading path, whereas the model response is virtually linear. But the value of δ that results in zero force during unloading is well predicted by the model and occurs at about $\delta = 0.5$ mm and 0.8 mm for $F_0 = 150$ N and 200 N, respectively.

7 Discussion

The proposed model is intended to model the rate- and history-dependent response of semi-crystalline polymers, and this includes stress relaxation. In general, stress relaxation in polymers is caused by time-dependent

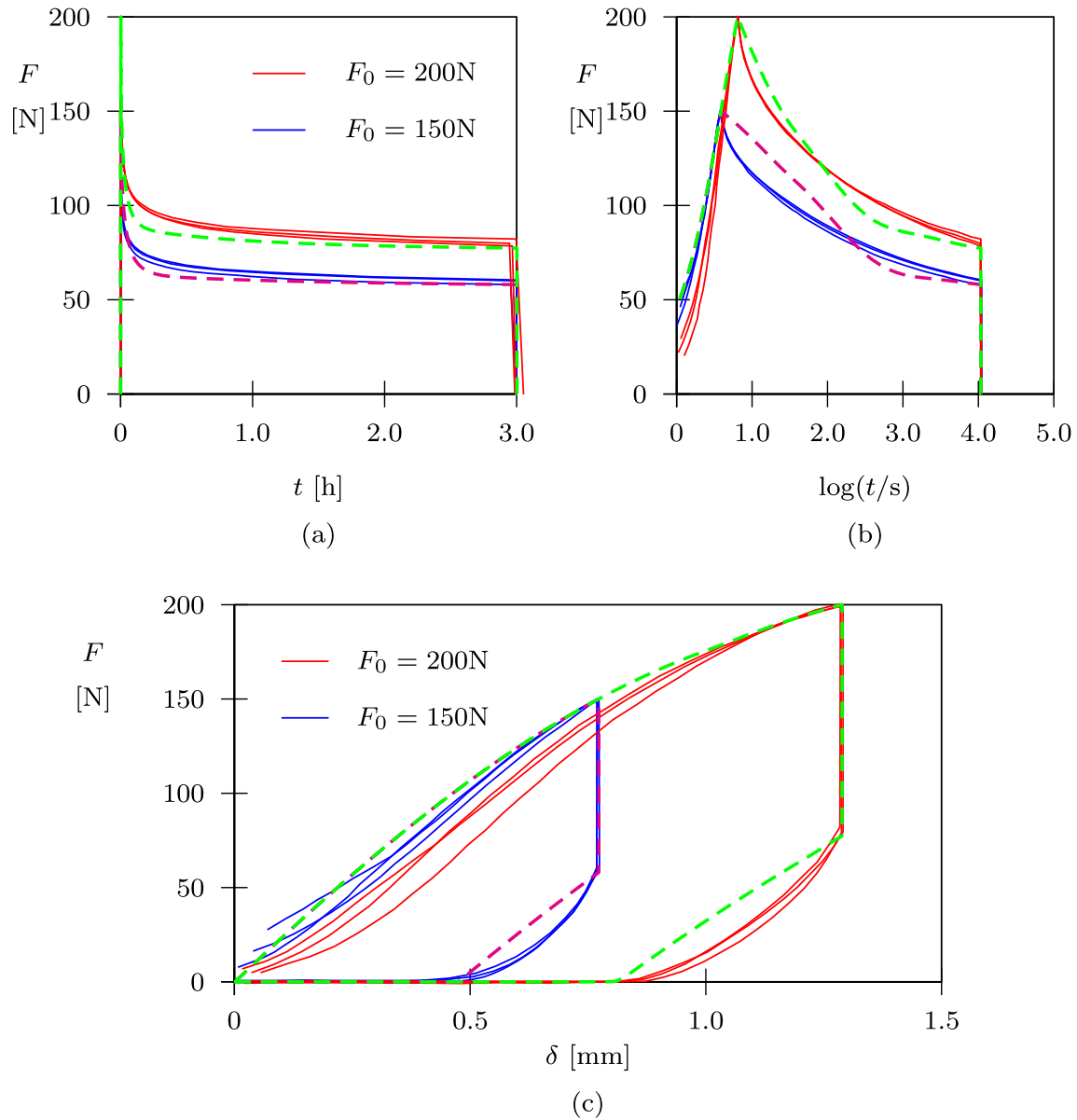**Fig. 9** Force relaxation of 3D geometry for two different initial loads, F_0. $F_0 = 150$ N: tests (solid blue lines) and model prediction (dashed magenta line), $F_0 = 200$ N: tests (solid red lines) and model prediction (dashed green line). **a** Force response versus time; **b** force response versus logarithm of time; **c** Force response versus load-line displacement (Color figure online)

rearrangements of the long, entangled polymer chains, where the polymer network reorganises itself in order to minimise the elastic energy. But the details of this process are more complicated. Doi and Edwards [15] suggested three basic mechanisms for stress relaxation in the amorphous phase, i.e. (a) relaxation between entanglements in order to re-establish a constant chain density, (b) chain retraction inside a deformed (and imagined) 'tube' in the material, and (c) chain disengagement from the 'tube' by a reptation process. These three steps would then be characterised by three different relaxation times. For semi-crystalline polymers, the situation is even more complex. Studies suggest that stress relaxation can be associated with the formation of microvoids in the amorphous phase in between the crystallites in the microstructure [12,56]. Furthermore, partial crystallisation of the amorphous phase is another mechanism that could cause stress relaxation [31,41, 64].

There are other models available in the literature that essentially set out to accomplish the same thing as the present model, and some of these were mentioned briefly in Sect. 1. An alternative Eulerian approach

was proposed by Simo [60]. However, in Simo's model, the yield criterion is formulated in stress space. Furthermore, the evolution of inelastic deformations is derived from a plastic potential and the principle of maximum plastic dissipation is applied in Simo's work, which is not the case in the present work. With regard to Lagrangian models, van Dommelen et al. [16] proposed a micromechanically motivated constitutive model for semi-crystalline polymers. van Dommelen et al. [16] make use of the multiplicative decomposition of the deformation gradient into elastic and inelastic parts, i.e. $\mathbf{F} = \mathbf{F}_e \mathbf{F}_i$. They use mixture theory to represent the contribution to the total stress from the two phases (crystalline and amorphous), and crystal plasticity is used for modelling the inelastic deformations of the crystalline phase. Ayoub et al. [6] also proposed a model for semi-crystalline polymers that is valid for finite strains and based on the multiplicative split of the deformation gradient. Ayoub et al. [6] propose a three-phase material where the total stress is produced by a 'molecular network resistance', an 'amorphous intermolecular resistance', and a 'crystalline intermolecular resistance'. This translates into three spring-dashpot units carrying the load in parallel, which among other things enables modelling of stress relaxation at different time scales. Other models exist that use more or less the same basic theoretical frameworks as the two models mentioned above. Both of these models are Lagrangian in the sense that their constitutive framework depends on the reference state through state variables like the total deformation gradient and the plastic/inelastic part of the deformation gradient. In contrast, the model proposed here is Eulerian in the sense that it only depends on state variables that are defined in the current state of the material. One attractive feature of the Eulerian framework is that the state variables are—at least in principle—measurable in the current state of the material. For example, the elastic strains (i.e. $\bar{\mathbf{B}}_e$ and J) can be measured directly by experimental techniques, such as diffraction methods. In contrast, total strains or plastic strains (in Lagrangian models) cannot be directly measured from the current state of the material. Furthermore, inelastic deformations are often taken to be incompressible, and another difference between the frameworks can be found in how this incompressibility is treated numerically. In numerical implementations of Lagrangian formulations of inelasticity, special numerical schemes must be used for ensuring that the plastic deformations remain incompressible ($\det\mathbf{F}_i = 1$). In the present Eulerian formulation, this issue simply never arises. The evolution laws in the present Eulerian formulation are also formulated in strain space, in contrast to the two Lagrangian formulations above, which are formulated in stress space. This also means that the numerical implementation of inelasticity becomes somewhat simpler.

The experimental results presented here can to some extent be compared to other studies. Drozdov and Christiansen [17] investigate the monotonic stress–strain response and also the stress relaxation of high-density polyethylene. At the strain rate 0.01/s, Drozdov and Christiansen [17] get an engineering stress peak of about 20 MPa. This stress peak is slightly lower than what was seen in the present study (23 MPa) at a slightly lower strain rate (0.0083/s). Drozdov and Christiansen [17] also perform stress relaxation tests, but they consider stress relaxation starting from an engineering stress of about 20 MPa, which is lower than in the present study. When starting a relaxation test at 20 MPa and then keeping the applied strain constant, the stress has relaxed to below 10 MPa after about 3000 s. The results from Drozdov and Christiansen [17] are consistent with the results in the present study.

The rate aspect of the relaxation behaviour in the model is primarily governed by the c_i-constants. For the present set of experiments, three relaxation terms ($n = 3$) were needed to describe the relaxation behaviour for all time ranges. The optimal values of these parameters were $c_1 = 1$/s, $c_2 = 0.05$/s, and $c_3 = 0.00003$/s. Inversion of these values gives an estimate of the time constants of the microstructural relaxation processes involved. Hence, the inverted values are $1/c_1 = 1$ s, $1/c_2 = 20$ s, and $1/c_3 \approx 33,000$ s≈ 9.3 h≈ 0.4 days. It is difficult to say in detail what the microstructural processes are, but this observation illustrates the complicated rate-dependence that these materials exhibit.

In the simulations of the 3D geometry, the simulations seemed to underestimate the initial stiffness of the structure. This could be due to the fact that the contact between the geometry and the rigid plates was taken to be friction-less. Introducing friction in the contact will make the simulated structure stiffer. Another reason why the simulation underestimated the structural stiffness could be that the inelasticity in the proposed model is pressure-independent. The hydrostatic stress usually has an impact on the inelastic flow in polymers, meaning that a positive hydrostatic stress facilitates inelastic flow whereas a negative hydrostatic stress has the opposite effect. Previous studies have also confirmed that there is such an effect in polyethylene [42, 62]. In the present study, the material model was calibrated by use of tensile tests, whereas the validation was performed by exposing the 3D geometry to compression loading. It could be expected that the model would then overestimate the relaxation of the 3D geometry compared to experiments. An overestimation of the relaxation was indeed observed but only after some time of relaxation. Overall, the present results suggest that

the relaxation properties of the present material in tension and compression are not too different, at least not within the stress and strain regimes considered here.

In the simulations, linear 8-node elements with incompatible modes were used. A limited mesh study was also carried out, where the element size in the regions with the largest deformations was decreased by a factor 2. This did not have any significant influence on the force response of the structure. In some regions of the 3D structure, the material undergoes large plastic deformations, and the material response is therefore close to near incompressible. In the element formulation in Abaqus, selectively reduced integration is applied, i.e. reduced integration is applied to the volumetric terms. This is done in order to prevent volumetric locking. Taken together, significant mesh-dependence should not be an issue in the present simulations.

In summary, the stress relaxation behaviour of HDPE has been studied both experimentally and theoretically. An Eulerian constitutive model for isotropic polymers was proposed. The model was able to describe the uniaxial tension results well, and it was also able to predict the behaviour of a 3D structure exposed to compression.

Declarations

Conflict of interest The authors declare that they have no competing interests.

Appendix A: Relation between Eulerian and Lagrangian formulations of kinematics

In the Lagrangian formulations, use is made of entities that are connected to the reference configuration of the material. Hence, the deformation gradient is defined as $\mathbf{F} = \partial \mathbf{x}/\partial \mathbf{X}$, where $\mathbf{x}$ and $\mathbf{X}$ are the current and reference position vectors, respectively. A common strategy is then to decompose the deformation gradient into elastic and inelastic parts, according to $\mathbf{F} = \mathbf{F}_e \mathbf{F}_i$, where $\mathbf{F}_e$ and $\mathbf{F}_i$ are the elastic and plastic/inelastic parts, respectively [11,30,37]. The elastic and plastic right Cauchy–Green deformation tensors are $\mathbf{C}_e = \mathbf{F}_e^T \mathbf{F}_e$ and $\mathbf{C}_i = \mathbf{F}_i^T \mathbf{F}_i$, respectively, and the elastic left Cauchy–Green deformation tensor is $\mathbf{B}_e = \mathbf{F}_e \mathbf{F}_e^T$. The velocity gradient $\mathbf{L}$ and the rate of deformation tensor $\mathbf{D}$ are defined by $\mathbf{L} = \dot{\mathbf{F}} \mathbf{F}^{-1} = \partial \mathbf{v}/\partial \mathbf{x}$ and $\mathbf{D} = (\mathbf{L} + \mathbf{L}^T)/2$, respectively.

The evolution of inelastic deformations can be modelled by the constitutive relation $\dot{\mathbf{C}}_i = \Gamma \mathbf{A}_r$, where $\mathbf{A}_r$ is a second-order tensor, and $\Gamma > 0$ is scalar function. The evolution of $\mathbf{C}_i$ can be expressed as

$$\dot{\mathbf{C}}_i = \overline{\dot{\mathbf{F}_i^T \mathbf{F}_i}} = \ldots = \mathbf{F}_i^T \mathbf{F}_e^{-1} \left(\mathbf{L} \mathbf{B}_e + \mathbf{B}_e \mathbf{L}^T - \dot{\mathbf{B}}_e \right) \mathbf{F}_e^{-T} \mathbf{F}_i. \tag{22}$$

Choosing $\mathbf{A}_r$ according to

$$\mathbf{A}_r = \mathbf{F}_i^T \left(\mathbf{I} - \frac{3\mathbf{C}_e^{-1}}{\mathbf{C}_e^{-1} : \mathbf{I}} \right) \mathbf{F}_i \tag{23}$$

leads to

$$\dot{\mathbf{B}}_e = \mathbf{L} \mathbf{B}_e + \mathbf{B}_e \mathbf{L}^T - \Gamma \left(\mathbf{B}_e - \frac{3\mathbf{I}}{\mathbf{B}_e^{-1} : \mathbf{I}} \right), \tag{24}$$

which can be seen as an evolution law for $\mathbf{B}_e$. The unimodular version of $\mathbf{B}_e$ is $\bar{\mathbf{B}}_e = \mathbf{B}_e / J^{2/3}$. Then, using the relation

$$\dot{\bar{\mathbf{B}}}_e = \frac{\dot{\mathbf{B}}_e}{J^{2/3}} - \frac{2}{3}(\mathbf{D} : \mathbf{I})\bar{\mathbf{B}}_e, \tag{25}$$

where incompressibility of inelastic deformations has been assumed, (24) can be recast into (2).

Appendix B: Numerical implementation of simple load cases

The material model behaviour is explored for three types of simple load cases: uniaxial tension, biaxial tension, and simple shear. In a uniaxial tension/compression test, the components of the deformation gradient and rate of deformation tensor are given by

$$\mathbf{F} = \begin{bmatrix} \lambda_1 & 0 & 0 \\ 0 & \lambda_2 & 0 \\ 0 & 0 & \lambda_2 \end{bmatrix}, \quad \mathbf{D} = \mathbf{L} = \dot{\mathbf{F}}\mathbf{F}^{-1} = \begin{bmatrix} \dfrac{\dot{\lambda}_1}{\lambda_1} & 0 & 0 \\ 0 & \dfrac{\dot{\lambda}_2}{\lambda_2} & 0 \\ 0 & 0 & \dfrac{\dot{\lambda}_2}{\lambda_2} \end{bmatrix}, \tag{26}$$

where a Cartesian coordinate system $X_1 - X_2 - X_3$ has been assumed, λ_1 is the stretch in the X_1-direction where the tension or compression is applied, and λ_2 denotes the transverse stretches in the traction-free X_2- and X_3-directions. The components of the unimodular elastic left Cauchy–Green deformation tensor are

$$\bar{\mathbf{B}}_e = \begin{bmatrix} \lambda_{e1}^2 & 0 & 0 \\ 0 & \dfrac{1}{\lambda_{e1}} & 0 \\ 0 & 0 & \dfrac{1}{\lambda_{e1}} \end{bmatrix}, \tag{27}$$

where λ_{e1} is the elastic stretch in the X_1-direction.

Time is discretized using a time step Δt, and discrete time steps are denoted by t_n, where $n = 0, 1, 2, 3, \ldots$ and $t_0 = 0$. Eqs. (2), (5), (19), (20), and (21) are discretized using an implicit scheme. Together with the boundary condition $T_{22} = T_{33} = 0$, the discretized problem to be solved can be stated as

$$J(t_n) - J(t_{n-1}) - \Delta t\,(\mathbf{D}(t_n) : \mathbf{I}) = 0, \tag{28}$$

$$\lambda_{e1}(t_n) - \lambda_{e1}(t_{n-1}) - \lambda_{e1}(t_n)D'_{11}(t_n)\Delta t +$$
$$\frac{\lambda_{e1}(t_n)(\lambda_{e1}^3(t_n) - 1)\Gamma(t_n)\Delta t}{1 + 2\lambda_{e1}^3(t_n)} = 0, \tag{29}$$

$$\mu(1/\lambda_{e1}(t_n) - \alpha_1(t_n)/3) + K(J(t_n) - 1)J(t_n) = 0. \tag{30}$$

For a given time step t_n and a given value $\lambda_1(t_n)$, (28)–(30) are solved for $\lambda_2(t_n)$, $\lambda_{e1}(t_n)$, and $J(t_n)$.

For the cases of biaxial tension and simple shear, the deformation gradient takes the forms

$$\mathbf{F} = \begin{bmatrix} \lambda_1 & 0 & 0 \\ 0 & \lambda_1 & 0 \\ 0 & 0 & \lambda_2 \end{bmatrix}, \quad \mathbf{F} = \begin{bmatrix} 1 & \gamma & 0 \\ 0 & 1 & 0 \\ 0 & 0 & \lambda_2 \end{bmatrix}, \tag{31}$$

respectively, where λ_1 and γ are the two prescribed deformation variables, and λ_2 responds to satisfy the boundary condition $T_{33} = 0$. The velocity gradient then takes the forms

$$\mathbf{L} = \begin{bmatrix} \dfrac{\dot{\lambda}_1}{\lambda_1} & 0 & 0 \\ 0 & \dfrac{\dot{\lambda}_1}{\lambda_1} & 0 \\ 0 & 0 & \dfrac{\dot{\lambda}_2}{\lambda_2} \end{bmatrix}, \quad \mathbf{L} = \begin{bmatrix} 0 & \dot{\gamma} & 0 \\ 0 & 0 & 0 \\ 0 & 0 & \dfrac{\dot{\lambda}_2}{\lambda_2} \end{bmatrix}, \tag{32}$$

and $\bar{\mathbf{B}}_e$ takes the forms

$$\bar{\mathbf{B}}_e = \begin{bmatrix} \lambda_{e1}^2 & 0 & 0 \\ 0 & \lambda_{e1}^2 & 0 \\ 0 & 0 & \dfrac{1}{\lambda_{e1}^4} \end{bmatrix}, \quad \bar{\mathbf{B}}_e = \begin{bmatrix} \beta_{11} & \beta_{12} & 0 \\ \beta_{12} & \beta_{22} & 0 \\ 0 & 0 & \beta_{33} \end{bmatrix}, \tag{33}$$

respectively, where $\beta_{33}(\beta_{11}\beta_{22} - \beta_{12}^2) = 1$. For the case of biaxial tension, the same set of equations, i.e. (28)–(30), needs to be solved, but (29) now instead takes the form

$$\lambda_{e1}(t_n) - \lambda_{e1}(t_{n-1}) - \lambda_{e1}(t_n)D'_{11}(t_n)\Delta t$$
$$+ \frac{\lambda_{e1}(t_n)(\lambda_{e1}^6(t_n) - 1)\Gamma(t_n)\Delta t}{2(2 + \lambda_{e1}^6(t_n))} = 0. \tag{34}$$

For simple shear, (29) expands to three equations, one equation each for the variables β_{11}, β_{22}, and β_{12}, respectively. These three equations are

$$\beta_{11}(t_n) - \beta_{11}(t_{n-1}) - 2\dot{\gamma}\beta_{12}(t_n)\Delta t + \frac{2}{3}\frac{\dot{\lambda}_2}{\lambda_2}\beta_{11}(t_n)\Delta t$$
$$+ \Gamma\left(\beta_{11}(t_n) - \frac{3\beta_{33}(t_n)}{1 + \beta_{33}^2(t_n)(\beta_{11}(t_n) + \beta_{22}(t_n))}\right)\Delta t = 0, \tag{35}$$

$$\beta_{22}(t_n) - \beta_{22}(t_{n-1}) + \frac{2}{3}\frac{\dot{\lambda}_2}{\lambda_2}\beta_{22}(t_n)\Delta t$$
$$+ \Gamma\left(\beta_{22}(t_n) - \frac{3\beta_{33}(t_n)}{1 + \beta_{33}^2(t_n)(\beta_{11}(t_n) + \beta_{22}(t_n))}\right)\Delta t = 0, \tag{36}$$

$$\beta_{12}(t_n) - \beta_{12}(t_{n-1}) - \dot{\gamma}\beta_{22}(t_n)\Delta t + \frac{2}{3}\frac{\dot{\lambda}_2}{\lambda_2}\beta_{12}(t_n)\Delta t$$
$$+ \Gamma\beta_{12}(t_n)\Delta t = 0. \tag{37}$$

Appendix C: Numerical implementation of material model

We consider a time step that starts at $t = t_n$, ends at $t = t_{n+1}$, and where the time increment is $\Delta t = t_{n+1} - t_n$. At $t = t_n$, the set of values $\{J(t_n), \bar{\mathbf{B}}_e(t_n), \kappa(t_n), \xi(t_n)\}$ is known, and the numerical integrator determines the values of these quantities at the end of the time step, i.e. $\{J(t_{n+1}), \bar{\mathbf{B}}_e(t_{n+1}), \kappa(t_{n+1}), \xi(t_{n+1})\}$. The numerical algorithm follows the works by Simo [59], Papes [45], and Rubin and Papes [54]. In the following, entities are assumed to be associated with time $t = t_{n+1}$ unless otherwise indicated.

The relative deformation gradient is defined as $\mathbf{F}_r(t) = \mathbf{F}(t)\mathbf{F}^{-1}(t_n)$. This entity satisfies the evolution equation and initial condition

$$\dot{\mathbf{F}}_r = \mathbf{L}\mathbf{F}_r, \quad \mathbf{F}_r(t_n) = \mathbf{I}. \tag{38}$$

The relative dilatation is $J_r = \det\mathbf{F}_r$. The exact solution of (5) is given by

$$J = J_r J(t_n). \tag{39}$$

The unimodular part of $\mathbf{F}_r$ is $\bar{\mathbf{F}}_r = J_r^{-1/3}\mathbf{F}_r$. The elastic trial solutions $\bar{\mathbf{B}}_e^*(t)$ and $\bar{\mathbf{B}}_e'^*(t)$ are defined by the expressions

$$\bar{\mathbf{B}}_e^*(t) = \bar{\mathbf{F}}_r\bar{\mathbf{B}}_e(t_n)\bar{\mathbf{F}}_r^T, \quad \bar{\mathbf{B}}_e'^*(t) = \bar{\mathbf{B}}_e^*(t) - \frac{1}{3}(\bar{\mathbf{B}}_e^*(t) : \mathbf{I})\mathbf{I}, \tag{40}$$

with $\bar{\mathbf{B}}_e'^*(t)$ satisfying the evolution equation and initial condition

$$\dot{\bar{\mathbf{B}}}_e'^* = \mathbf{L}\bar{\mathbf{B}}_e^* + \bar{\mathbf{B}}_e^*\mathbf{L}^T - \frac{2}{3}(\mathbf{D} : \bar{\mathbf{B}}_e^*)\mathbf{I} - \frac{2}{3}(\mathbf{D} : \mathbf{I})\bar{\mathbf{B}}_e'^*, \tag{41}$$

$$\bar{\mathbf{B}}_{\mathrm{e}}^{\prime *}(t_n) = \bar{\mathbf{B}}_{\mathrm{e}}^{\prime}(t_n). \tag{42}$$

The trial equivalent distortional elastic strain is given by

$$\gamma_{\mathrm{e}}^* = \frac{1}{2}\sqrt{\frac{3}{2}\bar{\mathbf{B}}_{\mathrm{e}}^{\prime *} : \bar{\mathbf{B}}_{\mathrm{e}}^{\prime *}}. \tag{43}$$

It can be shown that the deviatoric part of the evolution Eq. (2) becomes

$$\dot{\bar{\mathbf{B}}}_{\mathrm{e}}^{\prime} = \mathbf{L}\bar{\mathbf{B}}_{\mathrm{e}} + \bar{\mathbf{B}}_{\mathrm{e}}\mathbf{L}^{\mathrm{T}} - \frac{2}{3}(\mathbf{D} : \bar{\mathbf{B}}_{\mathrm{e}})\mathbf{I} - \frac{2}{3}(\mathbf{D} : \mathbf{I})\bar{\mathbf{B}}_{\mathrm{e}}^{\prime} - \Gamma\bar{\mathbf{B}}_{\mathrm{e}}^{\prime}. \tag{44}$$

Then, the evolution in (44) is approximated by

$$\dot{\bar{\mathbf{B}}}_{\mathrm{e}}^{\prime} \approx \dot{\bar{\mathbf{B}}}_{\mathrm{e}}^{\prime *} - \Gamma\bar{\mathbf{B}}_{\mathrm{e}}^{\prime}. \tag{45}$$

Using a backward Euler approximation of the derivative, the solution of (45) is written in the implicit form

$$\bar{\mathbf{B}}_{\mathrm{e}}^{\prime} = \lambda\bar{\mathbf{B}}_{\mathrm{e}}^{\prime *}, \tag{46}$$

with

$$\lambda = \frac{1}{1 + \Delta\Gamma}, \quad \Delta\Gamma = \Delta t\,\Gamma(t_{n+1}). \tag{47}$$

Then with the help of (6) and (46), it follows that

$$\gamma_{\mathrm{e}} = \lambda\gamma_{\mathrm{e}}^*. \tag{48}$$

The evolution of κ in (19) is approximated as

$$\kappa = \kappa(t_n) + \xi\Delta\Gamma_{\mathrm{vp}}, \tag{49}$$

where

$$\xi = \frac{\xi(t_n) + m\xi_{\mathrm{s}}\Delta\Gamma_{\mathrm{vp}}}{1 + m\Delta\Gamma_{\mathrm{vp}}} \tag{50}$$

is an implicit estimate of ξ based on (20), and $\Delta\Gamma_{\mathrm{vp}} = \Gamma_{\mathrm{vp}}\Delta t$. Furthermore, an implicit estimate of ζ_i can be obtained:

$$\zeta_i = \frac{\zeta_i(t_n) + n_i\zeta_{\mathrm{s},i}\Delta\varepsilon}{1 + n_i\Delta\varepsilon}, \tag{51}$$

where $\Delta\varepsilon = \dot{\varepsilon}\Delta t$. For the evaluation of $\dot{\varepsilon}$, an objective estimate of $\mathbf{D}$ is needed, and this estimate is given by

$$\mathbf{D} \approx \frac{1}{2\Delta t}(\mathbf{B}_{\mathrm{r}} - \mathbf{I}), \quad \mathbf{B}_{\mathrm{r}} = \mathbf{F}_{\mathrm{r}}\mathbf{F}_{\mathrm{r}}^{\mathrm{T}}. \tag{52}$$

We also have

$$\Delta\Gamma = \Delta\Gamma_{\mathrm{vp}} + \Delta\Gamma_{\mathrm{r}}, \tag{53}$$

where $\Delta\Gamma_{\mathrm{r}} = \Gamma_{\mathrm{r}}\Delta t$. The evolution of $\Delta\Gamma_{\mathrm{vp}}$ and $\Delta\Gamma_{\mathrm{r}}$ is given by

$$\Delta\Gamma_{\mathrm{vp}} = \underbrace{(a + b\dot{\varepsilon})\Delta t}_{a_{\mathrm{h}}}\underbrace{\langle\lambda\gamma_{\mathrm{e}}^* - \kappa\rangle}_{g_{\mathrm{vp}}} = a_{\mathrm{h}}\langle g_{\mathrm{vp}}\rangle, \tag{54}$$

and

$$\Delta\Gamma_{\mathrm{r}} = \sum_{i=1}^{n}c_i\Delta t\underbrace{\langle\lambda\gamma_{\mathrm{e}}^* - \zeta_i\rangle}_{g_{\mathrm{r},i}} = \underbrace{\lambda\gamma_{\mathrm{e}}^*\Delta t\sum_{i=1}^{n}c_i\Theta(g_{\mathrm{r},i})}_{d_{\mathrm{h}}} - \underbrace{\Delta t\sum_{i=1}^{n}c_i\zeta_i\Theta(g_{\mathrm{r},i})}_{e_{\mathrm{h}}}$$

$$= d_{\mathrm{h}}\lambda\gamma_{\mathrm{e}}^{*} - e_{\mathrm{h}}, \tag{55}$$

where $\Theta(x)$ is the Heaviside step function. When both (54) and (55) are active, these equations need to be solved for $\Delta\Gamma_{\mathrm{vp}}$ and $\Delta\Gamma_{\mathrm{r}}$ using a non-linear, iterative solution method. When $\Delta\Gamma_{\mathrm{vp}} = 0$, we have that $\Delta\Gamma = \Delta\Gamma_{\mathrm{r}}$ and $\lambda = 1/(1 + \Delta\Gamma_{\mathrm{r}})$, and the solution for $\Delta\Gamma_{\mathrm{r}}$ can be expressed on closed form according to

$$\Delta\Gamma_{\mathrm{r}} = -\frac{1 + e_{\mathrm{h}}}{2} + \sqrt{\frac{(1 + e_{\mathrm{h}})^2}{4} + d_{\mathrm{h}}\gamma_{\mathrm{e}}^{*} - e_{\mathrm{h}}}. \tag{56}$$

Once $\Delta\Gamma$ has been determined, $\bar{\mathbf{B}}_{\mathrm{e}}'(t_{n+1})$, $\xi(t_{n+1})$, and $\kappa(t_{n+1})$ can also be determined. Finally, α_1 can be determined from the third-order polynomial

$$\det\bar{\mathbf{B}}_{\mathrm{e}} = \det\left(\bar{\mathbf{B}}_{\mathrm{e}}' + \frac{\alpha_1}{3}\mathbf{I}\right) = \ldots$$
$$= \left(\frac{\alpha_1}{3}\right)^3 - \frac{1}{2}\left(\bar{\mathbf{B}}_{\mathrm{e}}' : \bar{\mathbf{B}}_{\mathrm{e}}'\right)\left(\frac{\alpha_1}{3}\right) + \det\bar{\mathbf{B}}_{\mathrm{e}}' = 1, \tag{57}$$

where $\bar{\mathbf{B}}_{\mathrm{e}}'$ is given by (46), and $\bar{\mathbf{B}}_{\mathrm{e}}(t_{n+1})$ has then also been defined.

An analytic expression for the algorithmic tangent modulus is also derived. In order to simplify the notation, a number of help variables, $(\bullet)_{\mathrm{h}}$, are introduced.

The updated Kirchhoff stress ultimately depends on $\mathbf{F}_{\mathrm{r}}$, and the variation of $\boldsymbol{\tau}$ is given by

$$\delta\boldsymbol{\tau} = \frac{\partial\boldsymbol{\tau}}{\partial\mathbf{F}_{\mathrm{r}}} : \delta\mathbf{F}_{\mathrm{r}} = \left(\frac{\partial\boldsymbol{\tau}}{\partial\mathbf{F}_{\mathrm{r}}}\mathbf{F}_{\mathrm{r}}^{\mathrm{T}}\right) : \left(\delta\mathbf{F}_{\mathrm{r}}\mathbf{F}_{\mathrm{r}}^{-1}\right). \tag{58}$$

The consistent tangent modulus, $\mathbb{C}$, can then be identified as

$$\mathbb{C} = \frac{1}{J}\frac{\partial\boldsymbol{\tau}}{\partial\mathbf{F}_{\mathrm{r}}}\mathbf{F}_{\mathrm{r}}^{\mathrm{T}}. \tag{59}$$

Differentiation of $\boldsymbol{\tau}$ yields

$$\frac{\partial\boldsymbol{\tau}}{\partial\mathbf{F}_{\mathrm{r}}} = \mu\frac{\partial\bar{\mathbf{B}}_{\mathrm{e}}'}{\partial\mathbf{F}_{\mathrm{r}}} + K(2J - 1)\mathbf{I} \otimes \frac{\partial J}{\partial\mathbf{F}_{\mathrm{r}}}. \tag{60}$$

Recalling that the current value of J is given by $J = J(t_n)J_{\mathrm{r}}$, it follows that

$$\frac{\partial J}{\partial\mathbf{F}_{\mathrm{r}}} = J(t_n)\frac{\partial J_{\mathrm{r}}}{\partial\mathbf{F}_{\mathrm{r}}} = J(t_n)J_{\mathrm{r}}\mathbf{F}_{\mathrm{r}}^{-\mathrm{T}} = J\mathbf{F}_{\mathrm{r}}^{-\mathrm{T}}, \tag{61}$$

and hence,

$$\frac{\partial J}{\partial\mathbf{F}_{\mathrm{r}}}\mathbf{F}_{\mathrm{r}}^{\mathrm{T}} = J\mathbf{I}. \tag{62}$$

Moreover, we have

$$\frac{\partial\bar{\mathbf{B}}_{\mathrm{e}}'}{\partial\mathbf{F}_{\mathrm{r}}} = \frac{\partial\left(\lambda\bar{\mathbf{B}}_{\mathrm{e}}'^{*}\right)}{\partial\mathbf{F}_{\mathrm{r}}} = \lambda\frac{\partial\bar{\mathbf{B}}_{\mathrm{e}}'^{*}}{\partial\mathbf{F}_{\mathrm{r}}} - \lambda\bar{\mathbf{B}}_{\mathrm{e}}' \otimes \frac{\partial\Delta\Gamma}{\partial\mathbf{F}_{\mathrm{r}}}. \tag{63}$$

Differentiation of (40) yields

$$\frac{\partial\bar{\mathbf{B}}_{\mathrm{e}}^{*}}{\partial\mathbf{F}_{\mathrm{r}}} = -\frac{2}{3}\bar{\mathbf{B}}_{\mathrm{e}}^{*} \otimes \mathbf{F}_{\mathrm{r}}^{-\mathrm{T}} + \frac{1}{J_{\mathrm{r}}^{2/3}}\frac{\partial\left(\mathbf{F}_{\mathrm{r}}\bar{\mathbf{B}}_{\mathrm{e}}(t_n)\mathbf{F}_{\mathrm{r}}^{\mathrm{T}}\right)}{\partial\mathbf{F}_{\mathrm{r}}}, \tag{64}$$

where

$$\frac{\partial\left(\mathbf{F}_{\mathrm{r}}\bar{\mathbf{B}}_{\mathrm{e}}(t_n)\mathbf{F}_{\mathrm{r}}^{\mathrm{T}}\right)}{\partial\mathbf{F}_{\mathrm{r}}} = (\mathbf{I} \ominus \mathbf{F}_{\mathrm{r}} + \mathbf{F}_{\mathrm{r}} \oplus \mathbf{I})\,\bar{\mathbf{B}}_{\mathrm{e}}(t_n), \tag{65}$$

and the notation $(\mathbf{Q} \ominus \mathbf{R})_{ijkl} = Q_{ik}R_{jl}$ and $(\mathbf{Q} \oplus \mathbf{R})_{ijkl} = Q_{il}R_{jk}$ has been introduced for convenience. It then follows that

$$
\begin{aligned}
\mathbb{D} &= \frac{\partial \bar{\mathbf{B}}_{\mathrm{e}}^{\prime *}}{\partial \mathbf{F}_{\mathrm{r}}} \mathbf{F}_{\mathrm{r}}^{\mathrm{T}} \\
&= \mathbf{I} \ominus \bar{\mathbf{B}}_{\mathrm{e}}^{*} + \bar{\mathbf{B}}_{\mathrm{e}}^{*} \oplus \mathbf{I} - \frac{2}{3} \left(\mathbf{I} \otimes \bar{\mathbf{B}}_{\mathrm{e}}^{*} + \bar{\mathbf{B}}_{\mathrm{e}}^{*} \otimes \mathbf{I} \right) + \frac{2}{9} \left(\bar{\mathbf{B}}_{\mathrm{e}}^{*} : \mathbf{I} \right) \mathbf{I} \otimes \mathbf{I}.
\end{aligned}
\tag{66}
$$

Differentiation of (54) and (55) yields

$$
\underbrace{\left(1 + a_{\mathrm{h}} \frac{\mathrm{d}\kappa}{\mathrm{d}(\Delta \Gamma_{\mathrm{vp}})} \right)}_{s_{\mathrm{h}}} \mathrm{d}(\Delta \Gamma_{\mathrm{vp}}) = b \Delta t g_{\mathrm{vp}} \mathrm{d}\dot{\varepsilon} + a_{\mathrm{h}} \lambda \mathrm{d}\gamma_{\mathrm{e}}^{*} - a_{\mathrm{h}} \lambda \gamma_{\mathrm{e}} \mathrm{d}(\Delta \Gamma),
\tag{67}
$$

$$
\mathrm{d}(\Delta \Gamma_{\mathrm{r}}) = d_{\mathrm{h}} \lambda \mathrm{d}\gamma_{\mathrm{e}}^{*} - q_{\mathrm{h}} \Delta t^{2} \mathrm{d}\dot{\varepsilon} - d_{\mathrm{h}} \lambda \gamma_{\mathrm{e}} \mathrm{d}(\Delta \Gamma),
\tag{68}
$$

where

$$
\frac{\mathrm{d}\kappa}{\mathrm{d}(\Delta \Gamma_{\mathrm{vp}})} = \frac{\xi(t_{n}) + 2m\xi_{\mathrm{s}} \Delta \Gamma_{\mathrm{vp}} - m(\kappa - \kappa(t_{n}))}{1 + m \Delta \Gamma_{\mathrm{vp}}},
\tag{69}
$$

$$
q_{\mathrm{h}} = \sum_{i=1}^{n} \frac{c_{i} n_{i} (\zeta_{\mathrm{s},i} - \zeta_{i})}{1 + n_{i} \Delta \varepsilon} \Theta(g_{\mathrm{r},i}).
\tag{70}
$$

Inserting the expressions in (67) and (68) into the differential version of (53) gives

$$
\underbrace{\left(1 + \lambda \gamma_{\mathrm{e}} \left(\frac{a_{\mathrm{h}} \Theta(g_{\mathrm{vp}})}{s_{\mathrm{h}}} + d_{\mathrm{h}} \right) \right)}_{u_{\mathrm{h}}} \mathrm{d}\Delta \Gamma = \lambda \underbrace{\left(\frac{a_{\mathrm{h}} \Theta(g_{\mathrm{vp}})}{s_{\mathrm{h}}} + d_{\mathrm{h}} \right)}_{z_{\mathrm{h}}} \mathrm{d}\gamma_{\mathrm{e}}^{*}
$$
$$
+ \underbrace{\left(\frac{b \Delta t \langle g_{\mathrm{vp}} \rangle}{s_{\mathrm{h}}} - q_{\mathrm{h}} \Delta t^{2} \right)}_{t_{\mathrm{h}}} \mathrm{d}\dot{\varepsilon},
\tag{71}
$$

which is also valid when $\Delta \Gamma_{\mathrm{vp}}$ and/or $\Delta \Gamma_{\mathrm{r}}$ are zero. The differentials $\mathrm{d}\gamma_{\mathrm{e}}^{*}$ and $\mathrm{d}\dot{\varepsilon}$ are given by

$$
\mathrm{d}\gamma_{\mathrm{e}}^{*} = \frac{3}{8\gamma_{\mathrm{e}}^{*}} \bar{\mathbf{B}}_{\mathrm{e}}^{\prime *} : \mathrm{d}\bar{\mathbf{B}}_{\mathrm{e}}^{\prime *},
\tag{72}
$$

$$
\mathrm{d}\dot{\varepsilon} = \frac{1}{3\Delta t^{2}\dot{\varepsilon}} (\mathbf{B}_{\mathrm{r}}' \mathbf{F}_{\mathrm{r}}) : \mathrm{d}\mathbf{F}_{\mathrm{r}},
\tag{73}
$$

where $\mathbf{B}_{\mathrm{r}}'$ is the deviatoric part of $\mathbf{B}_{\mathrm{r}}$. This gives

$$
\mathbf{H} = \frac{\partial \Delta \Gamma}{\partial \mathbf{F}_{\mathrm{r}}} \mathbf{F}_{\mathrm{r}}^{\mathrm{T}} = \frac{1}{u_{\mathrm{h}}} \left(\frac{3z_{\mathrm{h}}}{8\gamma_{\mathrm{e}}^{*}} \bar{\mathbf{B}}_{\mathrm{e}}' : \mathbb{D} + \frac{t_{\mathrm{h}}}{3\Delta t^{2}\dot{\varepsilon}} \mathbf{B}_{\mathrm{r}}' \mathbf{B}_{\mathrm{r}} \right).
\tag{74}
$$

Finally, the tangent tensor $\mathbb{C}$ can be expressed as

$$
\mathbb{C} = \frac{\mu \lambda}{J} \left(\mathbb{D} - \bar{\mathbf{B}}_{\mathrm{e}}' \otimes \mathbf{H} \right) + K(2J - 1) \mathbf{I} \otimes \mathbf{I}.
\tag{75}
$$

References

1. Abdul-Hameed, H., Messager, T., Zairi, F., Nait-Abdelaziz, M.: Large-strain viscoelastic–viscoplastic constitutive modeling of semi-crystalline polymers and model identification by deterministic/evolutionary approach. Comput. Mater. Sci. **90**, 241–252 (2014)
2. Abelen, A., Kroon, M.: Modelling of rate-dependent inelasticity and damage in semi-crystalline polymers using an Eulerian framework. Int. J. Eng. Sci. **193**, 103945 (2023)
3. Addiego, F., Dahoun, A., G'Sell, C., Hiver, J.M.: Characterization of volume strain at large deformation under uniaxial tension in high-density polyethylene. Polymer **47**, 4387–4399 (2006)
4. Argon, A.S., Galeski, A., Kazmierczak, T.: Rate mechanisms of plasticity in semi-crystalline polyethylene. Polymer **46**, 11798–11805 (2005)
5. Ayadi, W., Laiarinandrasana, L., Sai, K., et al.: Anisotropic (continuum damage mechanics)-based multi-mechanism model for semi-crystalline polymer. Int. J. Damage Mech. **27**, 357–386 (2018)
6. Ayoub, G., Zairi, F., Nait-Abdelaziz, M., Gloaguen, J.: Modelling large deformation behaviour under loading-unloading of semicrystalline polymers: application to a high density polyethylene. Int. J. Plast. **26**, 329–347 (2010)
7. Balieu, R., Lauro, F., Bennani, B., Delille, R., Matsumoto, T., Mottola, E.: A fully coupled elastoviscoplastic damage model at finite strains for mineral filled semi-crystalline polymer. Int. J. Plast. **51**, 241–270 (2013)
8. Barba, D., Arias, A., Garcia-Gonzalez, D.: Temperature and strain rate dependences on hardening and softening behaviours in semi-crystalline polymers: application to PEEK. Int. J. Solids Struct. **182**, 205–217 (2020)
9. Barriere, T., Gabrion, X., Holopainen, S.: A compact constitutive model to describe the viscoelastic-plastic behaviour of glassy polymers: comparison with monotonic and cyclic experiments and state-of-the-art models. Int. J. Plast. **122**, 31–48 (2019)
10. Bartczak, Z., Argon, Z.S., Cohen, R.E.: Texture evolution in large strain simple shear deformation of high density polyethylene. Polymer **35**, 3427–3441 (1994)
11. Boyce, M.C., Weber, G.G., Parks, D.M.: On the kinematics of finite strain plasticity. J. Mech. Phys. Solids **37**, 647–665 (1989)
12. Castagnet, S., Gacougnolle, J.L., Dang, P.: Correlation between macroscopical viscoelastic behaviour and micromechanisms in strained α polyvinylidene fluoride (PVDF). Mater. Sci. Eng. **A276**, 152–159 (2000)
13. Clausen, A.H., Polanco-Loria, M., Berstad, T., Hopperstad, O.S.: A constitutive model for thermoplastics with some applications. In: 8th European LS-DYNA Users Conference, Strasbourg (2011)
14. Cundiff, K., ayoub, G., Benzerga, A.: Modeling the viscoplastic behavior of a semicrystalline polymer. Int. J. Solids Struct. **254**, 111920 (2022)
15. Doi, M., Edwards, S.F.: The Theory of Polymer Dynamics, 1st edn. Clarendon Press, Oxford (1986)
16. van Dommelen, J.A.W., Parks, D.M., Boyce, M.C., Brekelmans, W.A.M., Baaijens, F.P.T.: Micromechanical modeling of the elasto-viscoplastic behavior of semi-crystalline polymers. J. Mech. Phys. Solids **10**, 389–398 (2003)
17. Drozdov, A.D., Christiansen, J.C.: Thermo-viscoelastic and viscoplastic behaviour of high-density polyethylene. Int. J. Solids Struct. **45**, 4274–4288 (2008)
18. Dusunceli, N., Colak, Z.: Modelling effects of degree of crystallinity on mechanical behavior of semicrystalline polymers. Int. J. Plast. **24**, 1224–1242 (2008)
19. El-Qoubaa, Z., Othman, R.: Strain rate sensitivity of polyetheretherketone's compressive yield stress at low and high temperatures. Mech. Mater. **95**, 15–27 (2016)
20. Felder, S., Holthusen, H., Hesseler, S., Pohlkemper, F., Simon, T.G.J.W., Reese, S.: Incorporating crystallinity distributions into a thermo-mechanically coupled constitutive model for semi-crystalline polymers. Int. J. Plast. **135**, 102751 (2020)
21. Galeski, A., Bartczak, Z., Argon, A.S., Cohen, R.E.: Morphological alterations during texture-producing plastic plane strain compression of high-density polyethylene. Macromolecules **25**, 5707–5718 (1992)
22. Garcia-Gonzalez, D., Zaera, R., Arias, A.: A hyperelastic-thermoviscoplastic constitutive model for semi-crystalline polymers: application to PEEK under dynamic loading conditions. Int. J. Plast. **88**, 27–52 (2017)
23. Ghatge, S., Yang, Y., Ahn, J.H., Hur, H.G.: Biodegradation of polyethylene: a brief review. Appl. Biol. Chem. **63**, 27 (2020)
24. Görtz, J.: Material characterization of long-term stress relaxation in a semi-crystalline polymer material—an experimental and numerical study. Master's thesis, Blekinge Institute of Technology (2021)
25. Hao, P., Laheri, V., Dai, Z., Gilabert, F.A.: A rate-dependent constitutive model predicting the double yield phenomenon, self-heating and thermal softening in semi-crystalline polymers. Int. J. Plast. **153**, 103233 (2022)
26. Hibbitt, D., Karlsson, B., Sorensen, P. (eds.): ABAQUS/Standard User's Manual, Version 6.16. Dassault Systemes SIMULIA Corp., Providence (2016)
27. Hong, K., Rastogi, A., Strobl, G.: A model treating tensile deformation of semicrystalline polymers: quasi-static stress–strain relationship and viscous stress determined for a sample of polyethylene. Macromolecules **37**, 10165–10173 (2004)
28. Katti, S.S., Schultz, J.M.: The microstructure of injection-molded semicrystalline polymers: a review. Polym. Eng. Sci. **22**, 1001–1017 (1982)
29. Krairi, A., Doghri, I.: A thermodynamically-based constitutive model for thermoplastic polymers coupling viscoelasticity, viscoplasticity and ductile damage. Int. J. Plast. **60**, 163–181 (2014)
30. Kröner, E.: Allgemeine Kontinuumstheorie der Versetzungen und Eigenspannungen. Arch. Ration. Mech. Anal. **4**, 273–334 (1960)
31. Kroon, M.: A constitutive model for strain-crystallising rubber-like materials. Mech. Mater. **42**, 873–885 (2010)
32. Kroon, M., Rubin, M.: Influence of thermal recovery on predictions of the residual mechanical state during melting and solidification. Mech. Mater. **141**, 103258 (2019)
33. Kroon, M., Rubin, M.: A simple scalar directional hardening model for the Bauschinger effect compared with a tensorial model. J. Mech. Mater. Struct. **15**, 511–537 (2020)
34. Kroon, M., Rubin, M.: An Eulerian constitutive model for the inelastic finite strain behaviour of isotropic semi-crystalline polymers. Eur. J. Mech. A/Solids **100**, 105004 (2023)

35. Kroon, M., Lindström, P., Rubin, M.: An Eulerian thermomechanical elastic–viscoplastic model with isotropic and directional hardening applied to computational welding mechanics. Acta Mech. **232**, 189–218 (2021)
36. Lee, B.J., Parks, D.M., Ahzi, S.: Micromechanical modeling of large plastic deformation and texture evolution in semi-crystalline polymers. J. Mech. Phys. Solids **41**, 1651–1687 (1993)
37. Lee, E.H.: Elastic–plastic deformation at finite strains. J. Appl. Mech. **36**, 27 (1968)
38. Li, D.S., Garmestani, H., Alamo, R.G., Kalidindi, S.R.: The role of crystallinity in the crystallographic texture evolution of polyethylenes during tensile deformation. Polymer **44**, 5355–5367 (2003)
39. Lin, L., Argon, A.S.: Review: structure and plastic deformation of polyethylene. J. Mater. Sci. **29**, 294–323 (1994)
40. Makki, M., ayoub, G., Pannier, C., Dargazany, r, Kadri, R., Abdelaziz, M.N., Nouri, H.: Micromechanical modeling of the visco-hyperelastic–viscoplastic behavior and fracture of aged semicrystalline polymers. Int. J. Non-Linear Mech. **155**, 104456 (2023)
41. Matthews, R., Ajji, A., Dumoulin, M., Prud'homme, R.: The effects of stress relaxation on the structure and orientation of tensile drawn poly(ethylene terephthalate). Polymer **41**, 7139–7145 (2000)
42. O'Connor, D.G., Findley, W.N.: Influence of normal stress on creep in tension and compression of polyethylene and rigid polyvinyl chloride copolymer. SPE Trans. **84**, 273–284 (1962)
43. Nikolov, S., Lebensohn, R., Raabe, D.: Self-consistent modeling of large plastic deformation, texture and morphology evolution in semi-crystalline polymers. J. Mech. Phys. Solids **54**, 1350–1375 (2006)
44. Onat, E.: The notion of state and its implications in thermodynamics of inelastic solids. In: Irreversible aspects of continuum mechanics and transfer of physical characteristics in moving fluids, pp. 292–314 . Springer (1968)
45. Papes, O.: Nonlinear continuum mechanics in modern engineering applications. Ph.D. thesis, ETH Zurich, DISS ETH NO 19956 (2013)
46. Parks, D., Ahzi, S.: Polycrystalline plastic deformation and texture evolution for crystals lacking five independent slip systems. J. Mech. Phys. Solids **38**, 701 (1990)
47. Pawlak, A., Galeski, A.: Plastic deformation of crystalline polymers: the role of cavitation and crystal plasticity. Macro-molecules **38**, 9688–9697 (2005)
48. Pouriayevali, H., Arabnejad, S., Guo, Y., Shim, V.: A constitutive description of the rate-sensitive response of semi-crystalline polymers. Int. J. Impact Eng. **62**, 35–47 (2013)
49. Qi, Z., Hu, N., Li, B., Zeng, D., Su, X.: Constitutive modeling for the elastic–viscoplastic behavior of high density polyethylene under cyclic loading. Int. J. Plast. **113**, 125–144 (2019)
50. Rae, P., Brown, E., Orler, E.: The mechanical properties of poly(ether-ether-ketone) (PEEK) with emphasis on the large compressive strain response. Polymer **48**, 598–614 (2007)
51. Reuvers, M.C., Kulkarni, S., Johlitz, M., Lion, A., Brepols, T., Reese, S.: A thermo-coupled constitutive model for semi-crystalline polymers at finite strains: application across scales. Tech. Mech. **43**, 211–219 (2023)
52. Rubin, M.B.: Plasticity theory formulated in terms of physically based microstructural variables—part I: theory. Int. J. Solids Struct. **31**, 2615–2634 (1994)
53. Rubin, M.B., Attia, A.V.: Calculation of hyperelastic response of finitely deformed elastic–viscoplastic materials. Int. J. Numer. Methods Eng. **39**, 309–320 (1996)
54. Rubin, M.B., Papes, O.: Advantages of formulating evolution equations for elastic–viscoplastic materials in terms of the velocity gradient instead of the spin tensor. J. Mech. Mater. Struct. **6**, 529–543 (2011)
55. Satouri, S., chatzigeorgiou, G., Benaarbia, A., Meraghni, F.: A theory of crack initiation and growth in viscoelastic media. Int. J. Damage Mech. **31**, 1639–1675 (2022)
56. Selles, N., Saintier, N., Laiarinandrasana, L.: Voiding mechanisms in semi-crystalline polyamide 6 during creep tests assessed by damage based constitutive relationships and finite elements calculations. Int. J. Plast. **86**, 112–127 (2016)
57. Serban, D., Weber, G., Marsavina, L., Silberschmidt, V., Hufenbach, W.: Tensile properties of semi-crystalline thermoplastic polymers: effects of temperature and strain rates. Polym. Test. **32**, 413–425 (2013)
58. Shojaei, A., Li, G.: Viscoplasticity analysis of semicrystalline polymers: a multiscale approach within micromechanics framework. Int. J. Plast. **42**, 31–49 (2013)
59. Simo, J.C.: A framework for finite strain elastoplasticity based on maximum plastic dissipation and the multiplicative decomposition. Part II: computational aspects. Comput. Methods Appl. Mech. Eng. **68**, 1–31 (1988)
60. Simo, J.C.: Algorithms for static and dynamic multiplicative plasticity that preserve the classical return mapping schemes of the infinitesimal theory. Comput. Methods Appl. Mech. Eng. **99**, 61–112 (1992)
61. Song, R., Berer, M., Muliana, A.: Mechanical responses of semi-crystalline thermoplastic polymers at various temperatures. Int. J. Solids Struct. **238**, 111398 (2022)
62. Spitzig, W.A., Richmond, O.: Effect of hydrostatic pressure on the deformation behaviour of polyethylene and polycarbonate in tension and in compression. Polym. Eng. Sci. **19**, 1129–1139 (1979)
63. Sreejith, P., Kannan, K., Rajagopal, K.: A thermodynamic framework for the additive manufacturing of crystallizing polymers. Part I: a theory that accounts for phase change, shrinkage, warpage and residual stress. Int. J. Eng. Sci. **183**, 103789 (2023)
64. Toki, S., Sics, I., Ran, S., Liu, L., Hsiao, B.S.: Molecular orientation and structural development in vulcanized polyisoprene rubbers during uniaxial deformation by in situ synchrotron X-ray diffraction. Polymer **44**, 6003–6011 (2003)
65. Uchida, M., Tada, N.: Micro-, meso- to macroscopic modeling of deformation behavior of semi-crystalline polymer. Int. J. Plast. **49**, 164–184 (2013)
66. Zeng, F., Grognec, P., Lacrampe, M.F., Krawczak, P.: A constitutive model for semi-crystalline polymers at high temperature and finite plastic strain: application to PA6 and PE biaxial stretching. Mech. Mater. **42**, 686–697 (2010)
67. Zeng, H., Song, L., Sun, H., Gu, J., Li, Z.: A thermoviscoelastic model for the one-way ad two-way shape memory effects of semi-crystalline polymers. Int. J. Eng. Sci. **185**, 103830 (2023)